Damage Prediction in Metal Forming Process Modeling and Optimization: Simplified Approaches

24

Ying-Qiao Guo, Yuming Li, Boussad Abbès, Hakim Naceur, and Ali Halouani

Contents

Y.-Q. Guo (✉) • Y. Li • B. Abbès • A. Halouani
Université de Reims Champagne-Ardenne, GRESPI/MPSE, Faculté des Sciences Exactes et Naturelles, Reims Cedex 2, France
e-mail: yq.guo@univ-reims.fr; yuming.li@univ-reims.fr; boussad.abbes@univ-reims.fr; alihalouani@yahoo.fr

H. Naceur
Université Lille Nord de France, Laboratoire LAMIH UMR 8201 CNRS, Valenciennes Cedex 9, France
e-mail: hakim.naceur@univ-valenciennes.fr

G. Z. Voyiadjis (ed.), *Handbook of Damage Mechanics*,
DOI 10.1007/978-1-4614-5589-9_41

Abstract

Some simplified numerical methods for damage predictions in metal forming process modeling and optimization are presented in this chapter. The incremental approaches including advanced damage models lead to accurate results, but the simulations are tedious and time-consuming. An efficient solving algorithm called *inverse approach* (IA) allows the fast modeling of forming processes in only one step between the known final part and the initial blank, avoiding the contact treatment and the incremental plastic integration. To improve the stress estimation in the IA, the so-called pseudo-inverse approach (PIA) has been developed. Some intermediate configurations are geometrically created and corrected by a free surface method to consider the deformation path, and the plastic integration based on the flow theory is carried out incrementally to consider the loading history. A simplified 3D strain-based damage model is coupled with the plasticity and implemented into a direct scalar integration algorithm of plasticity (without local iterations), which makes the plastic integration very fast and robust even for very large strain increments. These simplified approaches lead to very fast and useful numerical tools in the preliminary design and optimization.

Introduction

Nowadays, the forming industry needs to increase the product quality and to reduce the production costs and delay. The preliminary design of forming processes implies expensive trials-corrections on forming tools. The actual tendency is to use the numerical simulations in order to predict the forming feasibility (material flow, stresses, damage, etc.) and to optimize the process parameters and the tool geometry.

The numerical process modeling is a difficult task due to the involved complex phenomena: large strains, viscoplasticity, damage, contact-friction, thermal effects, etc. The incremental approaches with advanced damage models can give accurate results, but the simulation remains tedious and time-consuming; hence, it quickly becomes unfeasible in an optimization process. In this chapter, some simplified methods for damage modeling in metal forming process and optimization will be presented: (1) the fast forming algorithm IA which allows the calculation in only one step between the known final part and the initial blank, (2) the PIA which considers the loading path and improves significantly the stress estimation of the

IA, (3) a simplified 3D strain-based damage model and an efficient direct scalar integration algorithm of plasticity, and (4) the fast and robust forming process optimization using the above simplified approaches.

Two main approaches are widely used for the metal forming simulation: the incremental approach and the inverse approach (IA or one-step approach). The first one simulates the real multi-physic phenomena step by step, which makes it fairly accurate but very time-consuming. The second one exploits at maximum the knowledge of the final part shape; it performs the calculation from the known final configuration to the initial one in only one step to determine the strain and stress fields satisfying the equilibrium (Guo et al. 1990; Lee and Huh 1998, among others). The IA is based on two main assumptions: the tool actions are replaced by simplified nodal forces to avoid the contact-friction treatment, and the loading is supposed proportional to avoid the incremental plastic integration procedure. The strains and stresses are calculated by directly comparing the initial and final configurations. The IA is very fast and gives fairly good strain estimation. Nowadays, it is largely used as a valuable numerical tool in the preliminary design stages in various forming processes (stamping, hydroforming, etc.), in order to optimize the tool geometry and process parameters, such as the shape of initial metal sheet, the addendum surfaces, the drawbead sizes and positions, the holding forces, the springback compensation, etc. (Naceur et al. 2006; Dong et al. 2007; Azaouzi et al. 2008).

However, the IA cannot consider the loading history, leading to poor stress state estimation. The PIA has been developed to improve the stress estimation (Guo et al. 2004; Halouani et al. 2012a). Some intermediate configurations are geometrically created and mechanically corrected to take into account the deformation paths. The coupled damage–plasticity model is based on the flow theory of plasticity, and the plastic integration is carried out in an incremental form. The fast direct scalar algorithm of plasticity (DSAP) is used to speed up the procedure and avoid divergence problems in case of large strain increments. The PIA possesses not only the advantages of the IA (simple and fast), but also the advantages of the incremental approach (loading history, good stress estimation). Many research works based on the forward or backward methods have investigated the tool preform optimization (Kobayashi et al. 1989; Kim and Kobayashi 1990; Fourment et al. 1996), but too much computation time is required to carry out an optimization procedure. The PIA has been used for the automatic design and optimization of tool preforms. Genetic optimization algorithms and surrogate meta-models are adopted for the multi-objective optimization process in order to obtain the Pareto front (Halouani et al. 2012b).

Two main theories are extensively used to describe the ductile damage occurrence and its effect on the metal behavior. The first one was pioneered by Gurson (1977) and improved later by other researchers (Rousselier 1987, etc.). It is based on the micro-mechanisms of void nucleation, growth, and coalescence. It uses the void volume fraction as a "scalar" damage variable in the plastic potential in order to model the void effect on the plastic flow. The second one ignores the micro-defect mechanisms; it represents the damage effect on the overall elastoplastic

behavior of the material. The continuum damage mechanics (CDM) (Chaboche 1988; Lemaître and Chaboche 1990) uses a scalar or tensorial damage variables to represent the ductile defect evolution and their consequences on the other thermomechanical fields. This kind of CDM-based phenomenological approach has been widely applied to various metal forming and machining processes (Saanouni and Chaboche 2003).

There are two principal methods for the damage modeling: the uncoupled approach and the fully coupled one. The first one calculates the damage distribution with the stress and strain fields at the end of a FE analysis without taking into account its effect on other mechanical fields. It has been used by many authors to analyze damaged zones in the final workpiece (Hartley et al. 1989, among others). In some other works, the damage is used to find the forming limit strains in metal forming (Gelin et al. 1985; Cordebois and Ladevèze 1985). On the other hand, in the fully coupled approach, the damage effect is introduced directly into the constitutive equations, so it affects the other thermomechanical fields. The widely used models are based on the Gurson damage theory considering the void volume fraction evolution (Aravas 1986; Onate and Kleiber 1988; Picart et al. 1998). Other works are based on the continuum damage mechanics theory (CDM) (Lee et al. 1985; Zhu et al. 1992; Saanouni et al. 2000). A simplified approach based on Prandtl–Reuss plasticity model with nonlinear isotropic hardening is proposed in Mathur and Dawson (1987) and Brunet et al. (1996); the damage effect is taken into account by using the damage factor $(1 - D)$ on the stress vectors. Based on the thermodynamics of irreversible processes with state variables, an advanced approach aims to model the multi-physics coupling between the main thermomechanical phenomena including the isotropic and anisotropic damage (Mariage et al. 2002; Saanouni 2012, see also ▶ Chap. 25, "Ductile Damage in Metal Forming: Advanced Macroscopic Modeling and Numerical Simulation" of this volume).

In this chapter, a simplified model called 3D strain-based damage model (Lemaître and Chaboche 1990) and its applications in the IA and PIA will be presented. This ductile damage model is based on the dissipation potential and dedicated to the isotropic damage and hardening materials. The assumptions of the hardening saturation after the damage threshold and the constant triaxiality under proportional loading lead to a damage expression in terms of the equivalent plastic strain in a rate form, even in an integrated form. In the IA, an integrated constitutive equation is used to avoid the incremental plastic integration; the total damage expression is used to determine the damage distribution in the final workpiece (Cherouat et al. 2004). In the PIA, the damage effect is coupled with the plasticity by introducing the damage variable into the plasticity criterion; the damage rate expression is used to take account for their reciprocal effects (Guo et al. 2004).

In the PIA, the plastic strain increments are very large, so the classical iterative plastic integration based on the *return mapping algorithm* (Simo and Taylor 1986) requires much CPU time and may lead to divergence problems. A direct scalar algorithm of plasticity (DSAP) enables to directly performing the plastic integration without iterations (Li et al. 2007). The basic idea is to transform the unknown stress

vectors into the equivalent stresses which can be determined by using the tensile curve; then, the plastic multiplier λ can be directly calculated. The numerical results have shown very good agreement between the two algorithms, as well as the rapidity and robustness of the new DSAP.

Several examples will be presented to show the efficiency and limitations of the IA and PIA. The results are compared with those obtained by the classical incremental approach ABAQUS®/Explicit.

Inverse Approach for Sheet Forming Modeling

Basic Concept of the Inverse Approach

The IA has been proposed initially by Guo et al. (1990), for the estimation of the large elastoplastic strains encountered in the sheet forming process. The calculation is carried out from the known final workpiece to obtain the positions of material points in the initial blank (Fig. 1). Two main assumptions are adopted: the simplified tool action assumption to avoid the contact treatment and the proportional loading assumption to avoid the incremental plastic integration. This basic concept makes the IA very fast.

Since then, the IA has known numerous improvements, allowing the simulation of more complex 3D workpieces, including the friction, drawbeads, 3D anisotropy, rotation-free shell model, initial target solutions, spares solvers, etc. An important extension of the method has been done in order to deal with the tube hydroforming (Chebbah et al. 2011) and the cold forging (Halouani et al. 2010).

Formulation of the Inverse Approach

The IA formulation is presented below for the sheet forming and tube hydroforming by using a shell element. The FE formulation for axisymmetric cold forging can be found in Halouani et al. (2010).

The IA using the deformation theory of plasticity has different features comparing to the classical incremental approach: the known quantities are the final workpiece shape C, the FE mesh on C, and the thickness of the initial blank C^0, while the unknowns are the horizontal coordinates of the nodes in the initial

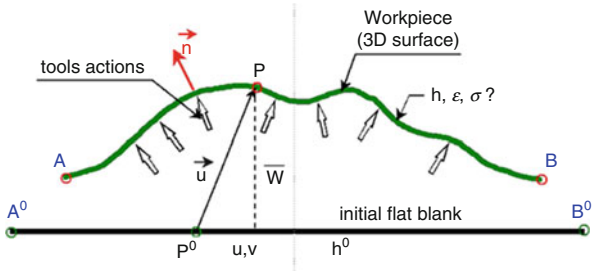

Fig. 1 Basic concept of the inverse approach

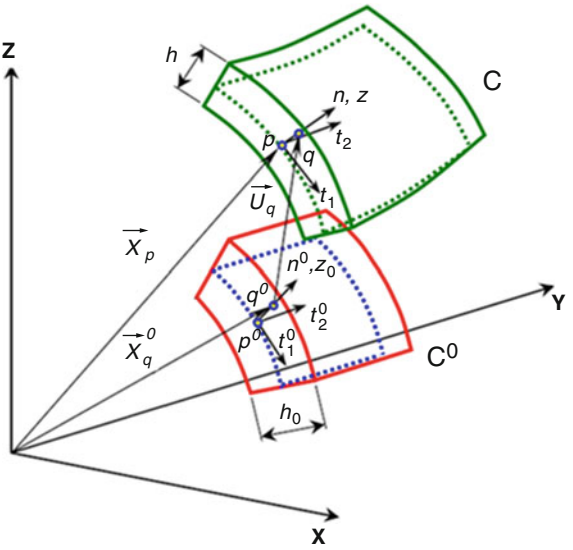

Fig. 2 Kinematics of 3D thin shell

flat blank and the thickness distribution in the final workpiece (Fig. 1). These unknowns are obtained by directly comparing C and C^0 in an iterative manner to satisfy the equilibrium conditions on C.

3D Shell Kinematics

Figure 2 illustrates the movement of a thin shell from its initial configuration C^0 to its final configuration C. p^0 is a material point on the shell mid-surface on C^0, q^0 is a point on the surface normal at p^0, and p and q are their final positions on C. Using the Kirchhoff assumption on the normal conservation, the following kinematic relations are obtained:

$$\boldsymbol{X}_{\boldsymbol{q}}^0 = \boldsymbol{X}_{\boldsymbol{p}}^0 + z^0\,\boldsymbol{n}^0 = \boldsymbol{X}_{\boldsymbol{p}} - \boldsymbol{U}_{\boldsymbol{p}} + \frac{z}{\lambda_3}\boldsymbol{n}^0; -\frac{h^0}{2} \le z^0 \le \frac{h^0}{2}; \quad z^0 = \frac{z}{\lambda_3} \tag{1}$$

$$\boldsymbol{X}_{\boldsymbol{q}} = \boldsymbol{X}_{\boldsymbol{p}} + z\,\boldsymbol{n}; -\frac{h}{2} \le z \le \frac{h}{2} \tag{2}$$

where $\boldsymbol{X}_p^0$ and $\boldsymbol{X}_p$ are the position vectors of p^0 and p, $\boldsymbol{U}_{\boldsymbol{p}}$ is the displacement vector between them, h^0 and h are the initial and final thicknesses, z^0 and z are the coordinates of q^0 and q through the thickness, λ_3 is the thickness stretch, and $\boldsymbol{n}^{\boldsymbol{0}}$ and $\boldsymbol{n}$ are the unit normal vectors at p^0 and p, respectively. It is noted that the final configuration is known and taken as reference.

Large Strain Measurement

Using two tangent vectors and the normal vector ($\boldsymbol{t_1}$, $\boldsymbol{t_2}$, $\boldsymbol{n}$) in p on the mid-surface of C, a local reference (x, y, z) is established:

$$\boldsymbol{t}_1 = \frac{\boldsymbol{X}_{p,x}}{\left\|\boldsymbol{X}_{p,x}\right\|} \quad ; \quad \boldsymbol{t}_2 = \frac{\boldsymbol{X}_{p,y}}{\left\|\boldsymbol{X}_{p,y}\right\|} \quad ; \quad \boldsymbol{n} = \boldsymbol{t}_1 \wedge \boldsymbol{t}_2 \tag{3}$$

The differentiation of Eqs. 1 and 2 gives the deformation gradient tensors with respect to the local reference (x, y, z):

$$d\boldsymbol{X}_q^0 = \left(\boldsymbol{F}_{\mathbf{x}}^0\right)^{-1} d\boldsymbol{x} \text{ with } \left(\boldsymbol{F}_{\mathbf{x}}^0\right)^{-1} = \left[\boldsymbol{X}_{p,x} - \boldsymbol{U}_{p,x} \vdots \boldsymbol{X}_{p,y} - \boldsymbol{U}_{p,y} \vdots \boldsymbol{n}^0/\lambda_3\right] \tag{4}$$

$$d\boldsymbol{X}_q = \boldsymbol{F}_{\mathbf{x}}\, d\boldsymbol{x} \text{ with } \boldsymbol{F}_{\mathbf{x}} = \left[\mathbf{X}_{p,x} + z\, \boldsymbol{n}_{,x} \vdots \boldsymbol{X}_{p,y} + z\, \boldsymbol{n}_{,y} \vdots \boldsymbol{n}\right] \tag{5}$$

The above two equations enable to obtain the inverse of deformation gradient tensor ($\boldsymbol{F}^{-1}$) between $d\boldsymbol{X}_q^0$ and $d\boldsymbol{X}_q$ and then the inverse of Cauchy–Green left tensor:

$$\boldsymbol{B}^{-1} = \boldsymbol{F}^{-T}\boldsymbol{F}^{-1} \tag{6}$$

The eigenvalues (λ_1^{-2}, λ_2^{-2}) of the tensor $\boldsymbol{B}^{-1}$ give the two in-plane principal stretches; the eigenvectors give their directions. The thickness elongation can be obtained by the incompressibility condition $\lambda_1\lambda_2\lambda_3 = 1$. The logarithmic principal strains in the final configuration C are given by

$$< \varepsilon_1\ \varepsilon_2\ \varepsilon_3 > = < \ln\lambda_1\ \ \ln\lambda_2\ \ \ln\lambda_3 > \tag{7}$$

Integrated Constitutive Law

In the IA, the proportional loading assumption is adopted to obtain an integrated constitutive law between the initial and final configurations. The loading history is ignored, leading to a total strain-stress law (see section "Simplified Plastic Ductile Damage Models and Direct Integration Algorithms" for more details):

$$\boldsymbol{\sigma} = \left[\boldsymbol{H}^{-1} + \left(\frac{1}{E_S} - \frac{1}{E}\right)\boldsymbol{P}\right]^{-1} \boldsymbol{\varepsilon} \tag{8}$$

where $\boldsymbol{\varepsilon}$ is the total strain vector, $\boldsymbol{H}$ is Hooke's elastic constitutive matrix, E_s is the secant modulus, E is Young's modulus, and $\boldsymbol{P}$ is the matrix defined by the von Mises isotropic criterion or Hill anisotropic criterion. The damage effect is uncoupled with the plasticity and evaluated as post-processing.

A non-quadratic anisotropic yield surface was proposed by Barlat et al. (2003) to deal with aluminum-based material parts:

$$f = \Phi' + \Phi'' - 2\overline{\sigma}_f^m = \left|X_1' - X_2'\right|^m + \left|2X_2'' - X_1''\right|^m + \left|2X_1'' - X_2''\right|^m - 2\overline{\sigma}_f^m = 0 \tag{9}$$

where $\overline{\sigma}_f^m$ is the updated effective yielding stress and the exponent m is mainly associated with the crystal structure of the material: a great m value corresponds to a small curvature radius at the rounded vertices of the yield surface. Typically, $m = 6$ and 8 are recommended, and X_1', X_2', X_1'', X_2'' are the principal values of the transformed deviatoric stresses $\boldsymbol{S}$:

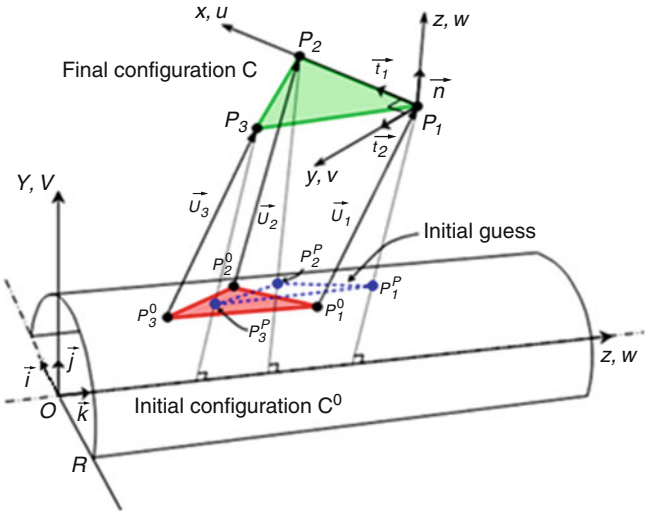

Fig. 3 3D mesh mapping onto the initial cylindrical tube surface

$$\begin{cases} \boldsymbol{X'} = \boldsymbol{C'}\,\boldsymbol{S} \\ \boldsymbol{X''} = \boldsymbol{C''}\,\boldsymbol{S} \end{cases} \tag{10}$$

where $\boldsymbol{C'}$ $\boldsymbol{C''}$ are the tensors of material parameters given in Barlat et al. (2003) and $\boldsymbol{\sigma}$ is the Cauchy stress tensor.

Using the normality law and the proportional loading assumption of the IA, the plastic strain rate can be integrated analytically, leading to a direct relationship between the total plastic strains and deviatoric stresses:

$$\boldsymbol{S} = \boldsymbol{H}^{p}\,\boldsymbol{\varepsilon}^{p} \tag{11}$$

Initial Solution Using Geometric Mapping Method

Several initial geometric guess techniques have been introduced by Naceur et al. (2002) to speed up the convergence of the static implicit solver in the IA. The authors proposed also other techniques for the treatment of vertical walls (balancing, opening, matrix condensing) which have been proven essential for complex 3D industrial parts.

To explain the basic concept of the initial solution, the geometric mapping method is described for the hydroforming of cylindrical tubes. The final mid-surface is discretized into triangular shell elements and mapped onto the initial cylindrical tube surface (Fig. 3).

Knowing the positions of the element nodes in the final configuration, the first guess can be achieved by radial projection of the nodes onto the initial cylindrical tube surface. These positions will be modified iteratively to meet the equilibrium in the final workpiece.

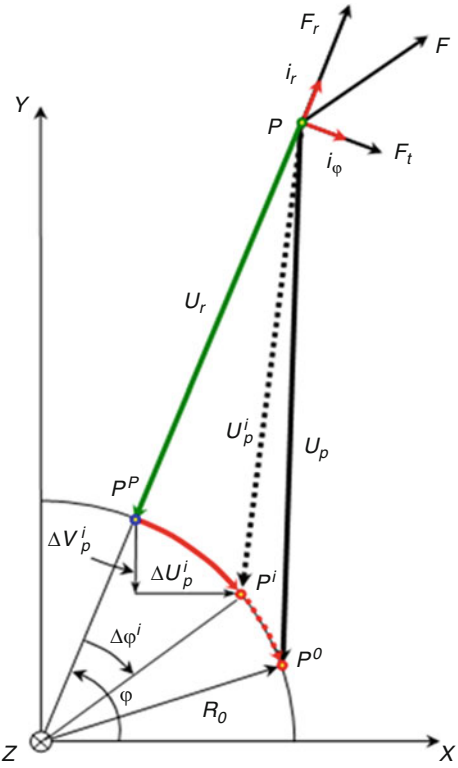

Fig. 4 Radial projection of point P and its movement on the tube surface

Since the mapping is made onto the known initial cylindrical surface, the radial displacement U_r of each node is known. The two other unknown displacements are axial and circumferential ones. The circumferential displacement is dependent on the unknown rotation angle $\Delta\varphi$. Its Cartesian components can be calculated as follows (Fig. 4):

$$\begin{array}{rcl} U_p^i & = & U_r \cos\varphi - \Delta U_p^i \\ V_p^i & = & U_r \sin\varphi + \Delta V_p^i \end{array} \text{ with } \begin{array}{rcl} \Delta U_p^i & = & R_0\left(\cos\left(\varphi - \Delta\varphi^i\right) - \cos\varphi\right) \\ \Delta V_p^i & = & R_0\left(\sin\left(\varphi - \Delta\varphi^i\right) - \sin\varphi\right) \end{array} \quad (12)$$

where R_0 is the radius of the tube mid-surface.

Variational Formulation

The discretization of the final shape of the desired workpiece is done by using a rotation-free shell element called DKTRF (Guo et al. 2002). This element is based on the membrane element CST and the plate element DKT6 (Batoz and Dhatt 1990). The DKTRF formulation involves the three neighboring elements in order to define the bending curvatures and build the element stiffness matrix without

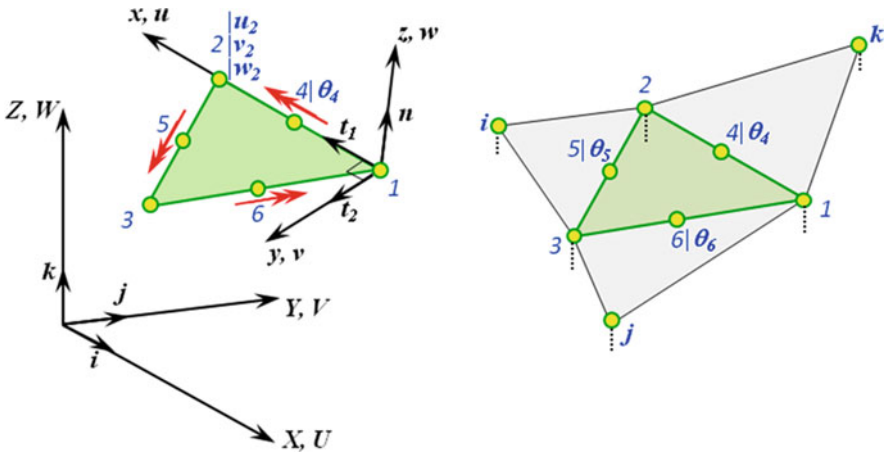

Fig. 5 DKT rotation-free triangular shell element

rotation degrees of freedom (Fig. 5). The resulting element has only three translations DOF per node.

Approximation of Strain Displacements

In the local reference of an element, the virtual membrane strains are expressed in terms of the two in-plane displacements along x and y:

$$\boldsymbol{e}^* = < \; u^*_{,x} \quad v^*_{,y} \quad u^*_{,y}+v^*_{,x} \; > \tag{13}$$

Linear approximations are used for u^* and v^* (constant strain triangle membrane element, CST) to obtain a constant membrane strain operator:

$$\boldsymbol{e}^* = \boldsymbol{B_m}\,\delta\left(\boldsymbol{u^*_n}\right)_m; \;\; (\boldsymbol{u_n})_m = \langle\, u_1 \quad v_1 \quad u_2 \quad v_2 \quad u_3 \quad v_3 \,\rangle \tag{14}$$

For the bending part, the rotations around the three element sides (θ_4, θ_5, θ_6) are expressed in terms of the transverse displacements of the six nodes (w_1, w_2, w_3, w_i, w_j, w_k, Fig. 5), the rotations normal to the three sides are expressed in terms of the transverse displacements of the three nodes (w_1, w_2, w_3, Fig. 5). Finally, a constant bending curvature operator is obtained, which is free from rotation degrees of freedom (Guo et al. 2002).

$$\boldsymbol{\chi}^* = \boldsymbol{B_f}\,\left(\boldsymbol{u^*_n}\right)_f; \;\; (\boldsymbol{u_n})_f = < \; w_1 \quad w_2 \quad w_3 \quad w_i \quad w_j \quad w_k \; > \tag{15}$$

Internal Force Vector

The principle of virtual work is used to establish the equilibrium on the final workpiece. The transverse shear effects are neglected for the thin sheet forming process. The virtual work of internal forces in an element is given by:

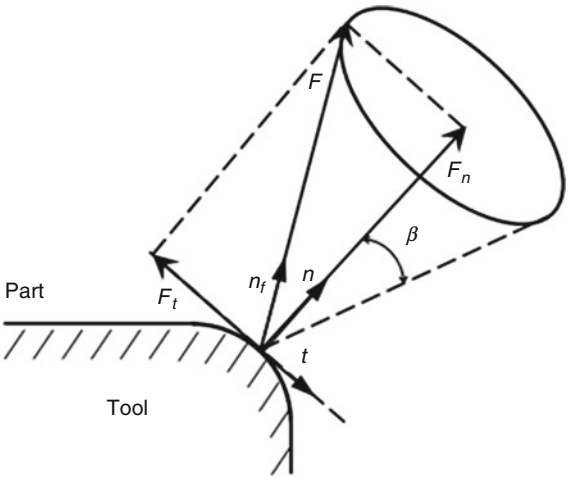

Fig. 6 Determination of the tool contact force by the friction cone

$$W_{\text{int}}^{e} = \int_{\text{V}^{\text{e}}} \boldsymbol{\varepsilon}^{*T}\, \boldsymbol{\sigma}\, dV = \boldsymbol{u}_{\boldsymbol{n}}^{*\text{T}} \boldsymbol{f}_{\text{int}}^{e} \tag{16}$$

By using the above FE approximation, the internal force vector in the global coordinate system is obtained:

$$W_{\text{int}}^{e} = \boldsymbol{U}_{\boldsymbol{n}}^{*\text{T}}\, \boldsymbol{F}_{\text{int}}^{e} \tag{17}$$

$$\boldsymbol{F}_{int}^{e} = \boldsymbol{T}^{\mathbf{T}} \int_{V^{e}} \left(\boldsymbol{B}_{\mathbf{m}}{}^{\text{T}} + z\, \boldsymbol{B}_{\mathbf{f}}{}^{\text{T}}\right) \quad \boldsymbol{\sigma}\, dV = A^{e}\, \boldsymbol{T}^{\text{T}} \left(\boldsymbol{B}_{\mathbf{m}}{}^{\text{T}} \boldsymbol{N} + \boldsymbol{B}_{\mathbf{f}}{}^{\text{T}} \boldsymbol{M}\right) \tag{18}$$

where $\boldsymbol{T}$ is the transformation matrix between the local and global references, $\boldsymbol{N}$ is the internal membrane force vector, and $\boldsymbol{M}$ is the internal bending–torsion moment vector.

External Force Vector

In the IA, the tool actions are simply represented by some external nodal forces to avoid the contact treatment. At a node, the resultant tool force $\boldsymbol{F}$ is composed of a normal pressure force $\boldsymbol{F}_n$ and a tangential friction force $\boldsymbol{F}_t$. $\boldsymbol{F}$ is situated on the friction cone surface defined by $\beta = arc\ \tan \mu$ (μ is friction coefficient, Fig. 6). Its direction $\boldsymbol{n}_f$ can be determined by the friction cone and the slide direction:

$$\boldsymbol{F} = F_n \boldsymbol{n} - F_t \boldsymbol{t} = \frac{F}{\sqrt{1+\mu^2}} (\boldsymbol{n} - \mu \boldsymbol{t}) = F \boldsymbol{n}_f \tag{19}$$

where $\boldsymbol{n}$ is the unit normal vector of the contour and $\boldsymbol{t}$ is the unit vector of the node displacement on the tangent direction.

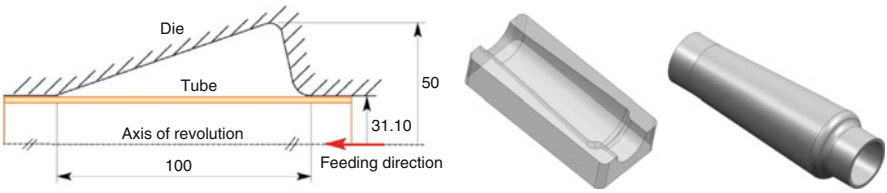

Fig. 7 Tube geometry and conical die

The value of $\boldsymbol{F}$ can be determined by the equilibrium condition at the contour. The following equilibrium equation can be established on a node k:

$$\boldsymbol{F}_{\text{ext}}^{k}\left(F^{k}\right)-\boldsymbol{F}_{\text{int}}^{i}=\left\{\begin{array}{c}F^{k}n_{X}^{k}\\F^{k}n_{Y}^{k}\\F^{k}n_{Z}^{k}\end{array}\right\}_{\text{ext}}-\left\{\begin{array}{c}F_{X}^{k}\\F_{Y}^{k}\\F_{Z}^{k}\end{array}\right\}_{\text{int}}=\left\{\begin{array}{c}0\\0\\0\end{array}\right\} \tag{20}$$

where $\left\langle\, n_{r}^{k} \quad n_{Z}^{k}\,\right\rangle^{T}=\boldsymbol{n}_{f}^{k}$ represents the resultant force direction at the node k. Then, the value of F^k and the nodal external force vector are obtained:

$$F^{k}=\left\langle\, n_{X}^{k} \quad n_{Y}^{k} \quad n_{Z}^{k}\,\right\rangle\left\{\begin{array}{c}F_{X}^{k}\\F_{Y}^{k}\\F_{Z}^{k}\end{array}\right\}_{\text{int}};\quad \boldsymbol{F}_{\text{ext}}^{k}=F^{k}\left\{\begin{array}{c}F_{X}^{k}\\F_{Y}^{k}\\F_{Z}^{k}\end{array}\right\}_{\text{ext}} \tag{21}$$

Application: Hydroforming of an Aluminum Alloy Conical Tube

The hydroforming of a conical tube has been studied by Jansson et al. (2008) (Fig. 7). The circumferential expansion attains 47.5 % from its original position. This is a difficult process because it requires a massive metal feeding into the expansion zone in order to avoid a burst fracture.

A 6-axis hydraulic press of 75 tons is used for the tube hydroforming. The axial feeding is provided on both sides of the tube. The whole device is instrumented with encoders and pressure sensors which allow the application of the axial feeding and pressure at any time during forming. Figure 8 shows the evolutions of the normalized pressure and feeding.

The tube is made of an aluminum alloy AA6063-T4. Both *Hill (1948)* and *Barlat (2000)* criteria are used. R_{00}, R_{45}, and R_{90} are the anisotropic coefficients; F, G, H, N, L are material parameters for *Hill* criterion; α_1–α_8 are the material parameters for *Barlat* criterion; they enable to consider the anisotropy in the evolution of the plastic flow surface for the case of uniaxial stress or biaxial stress state. The material data are as follows: $E = 68300$ MPa, $\nu = 0.3$, $\sigma_{00} = 78$ MPa, $\sigma_{45} = 76$ MPa, $\sigma_{90} = 74$ MPa, $\sigma_{11} = 23.4$ MPa, $\sigma_{22} = 85$ MPa, $R_{00} = 0.47$, $R_{45} = 0.12$, $R_{90} = 1.5$, $F = 0.43$, $G = 1.36$, $H = 0.64$, $N = 1.11$, $L = 0.43$, and α_1–$\alpha_8 = 0.72, 1.29, 0.99, 0.97, 1.03, 0.98, 0.16, 1.23$.

The curves of the pressure and feeding in function of time (Fig. 8) allow controlling the strain path, leading to a fully formed tube without bursting (Fig. 9). Firstly, the pressure is increased to 10 MPa with a moderate feeding in

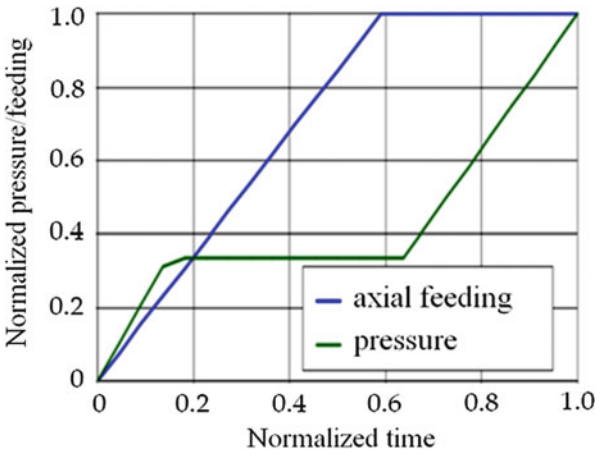

Fig. 8 Evolutions of the stroke (maximal value 33 mm) and pressure (maximal value 33 MPa) during forming

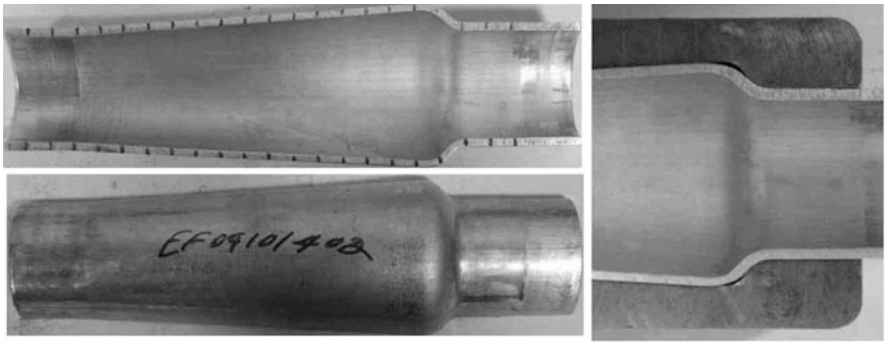

Fig. 9 Entirely formed conical tube

order to obtain a good compromise between the expansion and shortening; then, it is maintained constant while the axial feeding is increased until its maximum value of 33 mm. Secondly, the pressure is increased from 10 to 33 MPa to finish the expansion of the tube in the die.

In the numerical simulation, a quarter of the tube is discretized into 4536 DKTRF shell elements for the IA (Fig. 10). The same mesh is used for S3 shell elements in ABAQUS. The IA calculation uses only 38.7 s of CPU time, whereas the ABAQUS/Explicit calculation uses 275 s.

Figure 11 shows the thickness variation along the tube axis. The result obtained by the IA using the *Barlat (2000)* yielding criteria is in good agreement with that of ABAQUS using the same criterion.

It is noted that the thickness variation obtained by ABAQUS is closer to the experimental result than that by IA, especially at the die corner radius (at 80 and 210 mm). This can be explained by the fact that friction in the corner radii plays an important role, whereas the IA uses a simplified tooling action without loading history consideration.

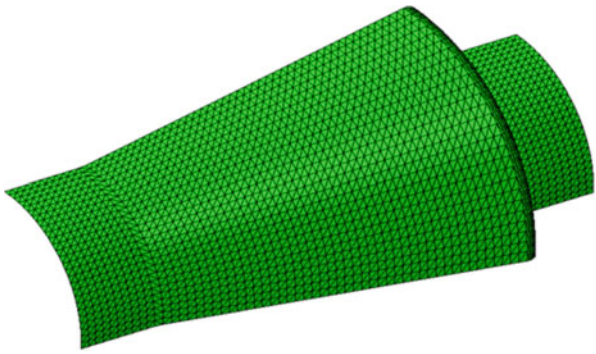

Fig. 10 Finite element mesh used for the IA calculation

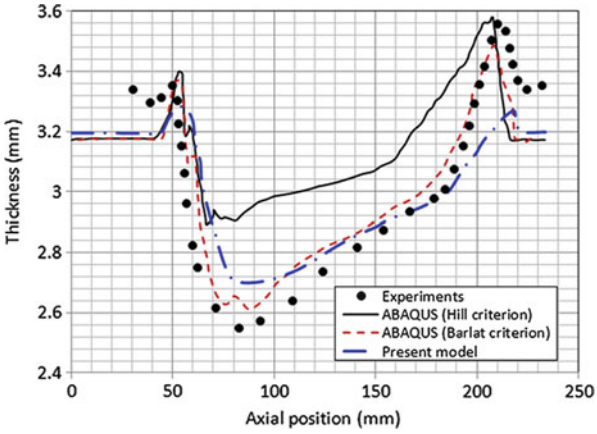

Fig. 11 Comparison of thickness variations along the tube axis

Pseudo-inverse Approach for Forming Process Modeling

In the IA, only the initial and final configurations are considered to calculate the total strains and then the total stresses by using the deformation theory of plasticity. This allows obtaining good strain estimation, but poor stress estimation. In the PIA, some *realistic* intermediate configurations are introduced to consider the deformation paths, and the incremental flow theory of plasticity with the damage is adopted to take into account the loading history.

Creation of Intermediate Configurations

Creation of Intermediate Configurations for Sheet Forming Modeling

In a 3D sheet forming process, since the final part shape and the tools are known, the intermediate configurations can be approximately generated by a geometrical

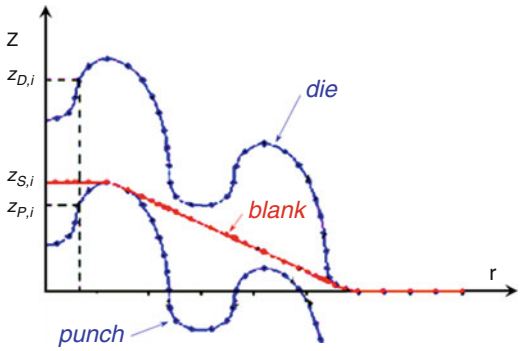

Fig. 12 Creation of an intermediate configuration by minimizing sheet surface

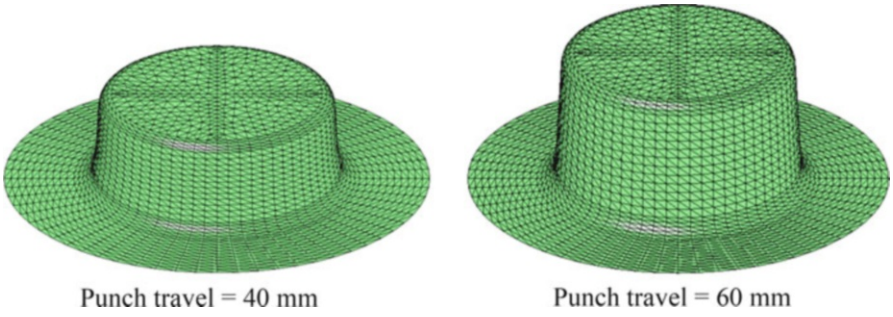

Fig. 13 Generation of the 3D mesh of an intermediate sheet configuration

method before the mechanical calculation (Guo et al. 2004). Considering a sheet as a stretched membrane in accordance with the tools (Fig. 12), its shape can be determined by minimizing its total surface:

$$J = Min \sum_{e} A_e; \quad z_{P,i} \leq z_{S,i} \leq z_{D,i} \tag{22}$$

where A_e is an element area and z_P, z_S, and z_D are the nodal vertical positions of a point on the punch, sheet, and die, respectively.

For a 2D or axisymmetric part, the minimization of the sheet surfaces can be done by using its profile. In a 3D case, the workpiece is divided into several sectors, and each of them is treated as a 2D case; all sectors are assembled together by linear interpolation (Fig. 13).

It is noted that the nodes having the same number in the intermediate and final meshes do not represent the same material point; a transfer of the strain and stress fields should be done between these two independent meshes.

Free Surface Method for Axisymmetric Cold Forging

In the axisymmetric cold forging process, some intermediate configurations are generated to consider the deformation history. An intermediate configuration is

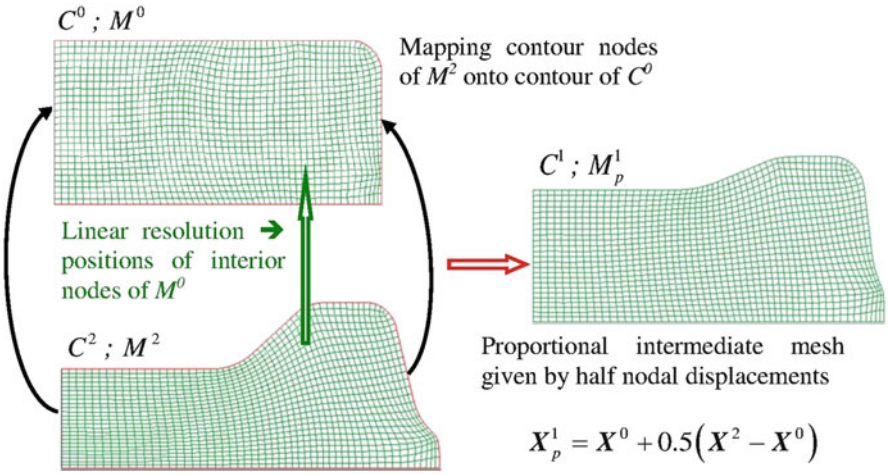

Fig. 14 Proportional intermediate mesh for PIA in a two-stage forging

created geometrically and then corrected by using a free surface method (Halouani et al. 2012), in order to obtain the free surface shape satisfying the equilibrium conditions.

Geometric Proportional Intermediate Configurations

In the PIA, the FE mesh M^2 is created on the known final part C^2. The contour of the initial billet C^0 is also known. For a two-step forging process, a geometric proportional configuration is generated as follows (Fig. 14):

1. The contour nodes of M^2 are mapped onto the contour of C^0, and the positions of the interior nodes on C^0 are determined by a linear solution on M^2 with the imposed contour node displacements from C^2 to C^0 as boundary conditions.
2. The intermediate mesh M^1_p is created by using a geometric proportional interpolation:

$$\boldsymbol{X}^1_p = \boldsymbol{X}^0 + 0.5\left(\boldsymbol{X}^2 - \boldsymbol{X}^0\right) \tag{23}$$

   where $\boldsymbol{X}^0$, $\boldsymbol{X}^1_p$, and $\boldsymbol{X}^2$ are the nodal position vectors of the meshes on the initial, intermediate, and final configurations.
3. The kinematic conditions of the mesh M^1_p are checked. If some nodes penetrate into the tool, they are mapped back on the tool contour (Fig. 15).

Determination of the Free Surface of an Intermediate Configuration

Once the kinematically admissible intermediate mesh is obtained, an inverse calculation is carried out between M^1_p and M^0. The mesh M^0 is fixed, the mesh M^1_p is taken as a reference to calculate the strains and stresses; M^1_p is modified iteratively in order to satisfy the equilibrium and contact conditions. Thus, the free surface

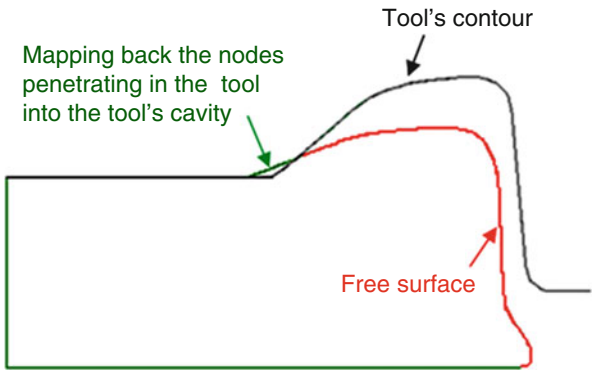

Fig. 15 Kinematically admissible free surface

shape is determined at the end of the equilibrium loop. The boundary conditions of M_p^1 are defined as follows (Fig. 15):

- If the nodal force points outward from the billet ($F_n > 0$, false), the node should be on a free surface having the boundary conditions: $U \neq 0$, $V \neq 0$, $\sigma_n = 0$, $\tau_n = 0$.
- If the nodal force points toward inside ($F_n < 0$), the contact conditions between the billet and tool give the tangent displacement $U_i' \neq 0$ and the normal one $V_i' = 0$ on the tool contour.
- Then, the IA calculation is performed and the nodal positions are updated in the intermediate configuration M_p^1.

The above operations are repeated in the equilibrium iteration loop until the convergence. The incompressibility condition, the contact condition, and the equilibrium at the free surface enable to obtain the mesh M_1^1 (superscript means step 1, subscript means configuration C^1) representing the real shape of the free surface.

Figure 16 shows the intermediate configurations obtained by the geometric proportional method, the PIA free surface method and ABAQUS® at the sixth step for a PIA calculation. It is noted that the proportional mesh is a good initial mesh but has a notable difference compared to the ABAQUS mesh (zones A and B). The realistic mesh obtained by the free surface method is very close to the ABAQUS® mesh.

Calculation of Large Strain Increments

The calculation of the large logarithmic strains in the IA is done in one step by directly comparing the initial billet and the final part (Halouani et al. 2010). A similar calculation is kept in the PIA but between two successive configurations.

For an axisymmetric problem, each material point moves in its meridian plane; the displacement field is therefore independent of the circumferential coordinate. The movement of a material point between two successive configurations C^{n-1} and

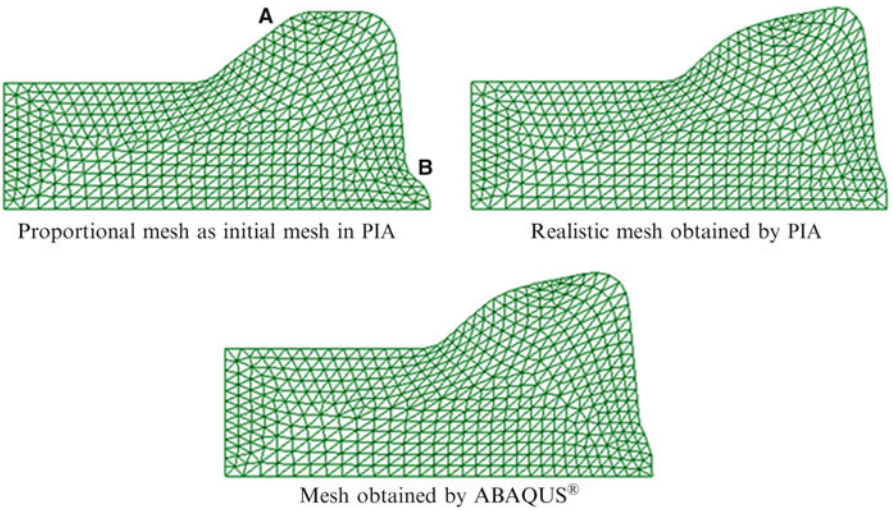

Fig. 16 Proportional mesh, PIA free surface mesh, and ABAQUS® mesh at step 6

C^n is expressed by $\boldsymbol{r}^{n-1} = \boldsymbol{r} - \Delta\boldsymbol{u}$ where $\boldsymbol{r}^{n-1}$ and $\boldsymbol{r}$ are the position vectors in C^{n-1} and C^n and $\Delta\boldsymbol{u}$ is the displacement increment vector in the radial plane.

Taking the known configurations C^n as reference, the inverse deformation gradient tensor is defined in the reference (r, z) as follows:

$$d\boldsymbol{r}^{n-1} = \frac{\partial \boldsymbol{r}^{n-1}}{\partial \boldsymbol{r}} d\boldsymbol{r} = \left(\boldsymbol{I} - \frac{\partial \Delta\boldsymbol{u}}{\partial \boldsymbol{r}}\right) d\boldsymbol{r} = \boldsymbol{F}_{\mathrm{L}}^{-1} d\boldsymbol{r} \tag{24}$$

with

$$\boldsymbol{F}_{\mathrm{L}}^{-1} = \begin{bmatrix} 1 - \Delta u_{,r} & 0 & -\Delta u_{,z} \\ 0 & 1 - \dfrac{\Delta u}{r} & 0 \\ -\Delta w_{,r} & 0 & 1 - \Delta w_{,z} \end{bmatrix} \tag{25}$$

The inverse of the Cauchy–Green left tensor is defined by:

$$(d\boldsymbol{r}^n)^{\mathrm{T}} d\boldsymbol{r}^n = d\boldsymbol{r}^{\mathrm{T}} \boldsymbol{F}_{\mathrm{L}}^{-\mathrm{T}} \boldsymbol{F}_{\mathrm{L}}^{-1} d\boldsymbol{r} = d\boldsymbol{r}^{\mathrm{T}} \boldsymbol{B}^{-1} d\boldsymbol{r} \tag{26}$$

$$\boldsymbol{B}^{-1} = \begin{bmatrix} (1 - \Delta u_{,r})^2 + (\Delta w_{,r})^2 & 0 & -\Delta u_{,z}(1 - \Delta u_{,r}) - \Delta w_{,r}(1 - \Delta w_{,z}) \\ 0 & (1 - \frac{\Delta u}{r})^2 & 0 \\ -\Delta u_{,z}(1 - \Delta u_{,r}) - \Delta w_{,r}(1 - \Delta w_{,z}) & 0 & (1 - \Delta w_{,z})^2 + (\Delta u_{,z})^2 \end{bmatrix} \tag{27}$$

The eigenvalues ($\Delta\lambda_1^{-2}$, $\Delta\lambda_2^{-2}$, $\Delta\lambda_3^{-2}$) of the tensor $\boldsymbol{B}^{-1}$ give the three principal elongations ($\Delta\lambda_1$, $\Delta\lambda_2$, $\Delta\lambda_3$), and the eigenvectors define the directions of these principal elongations:

$$\boldsymbol{B}^{-1} = \boldsymbol{M}\begin{bmatrix} \lambda_1^{-2} & 0 & 0 \\ 0 & \lambda_2^{-2} & 0 \\ 0 & 0 & \lambda_3^{-2} \end{bmatrix}\boldsymbol{M}^T \tag{28}$$

Then, the principal logarithmic strain increment is given by

$$\Delta\boldsymbol{\varepsilon} = \begin{Bmatrix} \Delta\varepsilon_1 \\ \Delta\varepsilon_2 \\ \Delta\varepsilon_3 \end{Bmatrix} = \begin{Bmatrix} \ln\Delta\lambda_1 \\ \ln\Delta\lambda_2 \\ \ln\Delta\lambda_3 \end{Bmatrix} \tag{29}$$

The large logarithmic strains in the reference (r, z) can be obtained by the following transformation (Batoz and Dhatt 1990):

$$\Delta\boldsymbol{\varepsilon} = \begin{Bmatrix} \Delta\varepsilon_r \\ \Delta\varepsilon_\theta \\ \Delta\varepsilon_z \\ \Delta\gamma_{rz} \end{Bmatrix} = \begin{bmatrix} \cos^2\varphi & 0 & \sin^2\varphi \\ 0 & 1 & 0 \\ \sin^2\varphi & 0 & \cos^2\varphi \\ 2\sin\varphi\cos\varphi & 0 & -2\sin\varphi\cos\varphi \end{bmatrix}\begin{Bmatrix} \Delta\varepsilon_1 \\ \Delta\varepsilon_2 \\ \Delta\varepsilon_3 \end{Bmatrix} \tag{30}$$

where φ is the angle from the r axis to the first principal strain axis.

In the PIA, the inverse calculation is carried out between two successive configurations using the strains and stresses obtained in the previous step. At the step n-1, the FE mesh is created on C^{n-1} and modified by the free surface method; at the step n, the mesh is created on C^n and mapped on C^{n-1} for the inverse calculation. These two meshes on C^{n-1} are completely independent, so a transfer of the strain and stress fields should be done between them.

Direct Integration of Plasticity and Damage for Large Strain Increments

The return mapping algorithm (RMA) (Simo and Taylor 1986) is the most widely used iterative scheme. It is considered as an efficient method for the plastic integration, but it consumes much computation time because of numerous integration points in whole structure and numerous iterations in the global equilibrium loop. Moreover, this iterative scheme may cause divergence problems for large strain increments. The new algorithm called direct scalar algorithm of plasticity (DSAP) proposed by Li et al. (2007) is very fast and robust without local iterative loop. The basic idea of the DSAP is to transform the constitutive equations with unknown stress vectors into a scalar equation in terms of equivalent stresses which can be obtained by using the tensile curve, leading to a direct solution to obtain the plastic multiplier $\Delta\lambda$ (see section "► Simplified Plastic Ductile Damage Models and Direct Integration Algorithms").

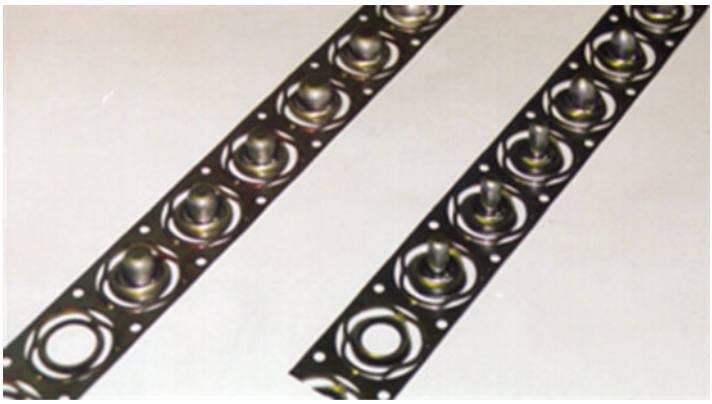

Fig. 17 Photo of an axisymmetric pot stamping in three stages

Numerical Results: Simulation of a Three-Stage Stamping Process

An axisymmetric pot is realized by three successive stamping stages (Fig. 17). The stamping is carried out continuously on a sheet band. The geometrical dimensions are given in Fig. 18. The first two stages are designed to obtain the biaxial strain states below the FLC curve.

The sheet is cut by six arc knives before the stamping to facilitate the sheet draw-in. In the third stage, the pot with a large diameter should be pushed by the punch into the die of smaller diameter; this implies the bending–unbending effect. The intermediate shape of the part is determined by the geometrical relations between the sheet and the tools (Fig. 19).

The material of the sheet is the steel DC04, its thickness is 1 mm. The part heights at the three stages are 13, 15 and 15 mm, respectively. The friction coefficient is 0.144 between the sheet and die.

In stage 1, a good agreement of the thickness distributions is obtained between the numerical results of the PIA and the experimental results of CETIM. It is found that the maximal thickness thinning is 13.2 % for CETIM and 10.6 % for PIA. The comparison of the FLD (forming limit diagram) shows also a good coherence between the numerical and experimental strain states.

In stage 2, the thickness distributions obtained by CETIM and PIA are also very similar. The maximal thinning is situated at the upper radius of the part. The maximal values are 17.4 % by CETIM and 15.3 % by PIA (Fig. 20). The experimental FLD points correspond well to those obtained by the PIA (Fig. 21). It is noted that only a small zone on the part has been measured in the experimental test.

In stage 3, the difference of the thickness distributions becomes notable between the numerical and experimental results: 30.3 % of thinning for PIA but 40.7 % for CETIM (Fig. 22). The reason of this error is due to the assumption on the

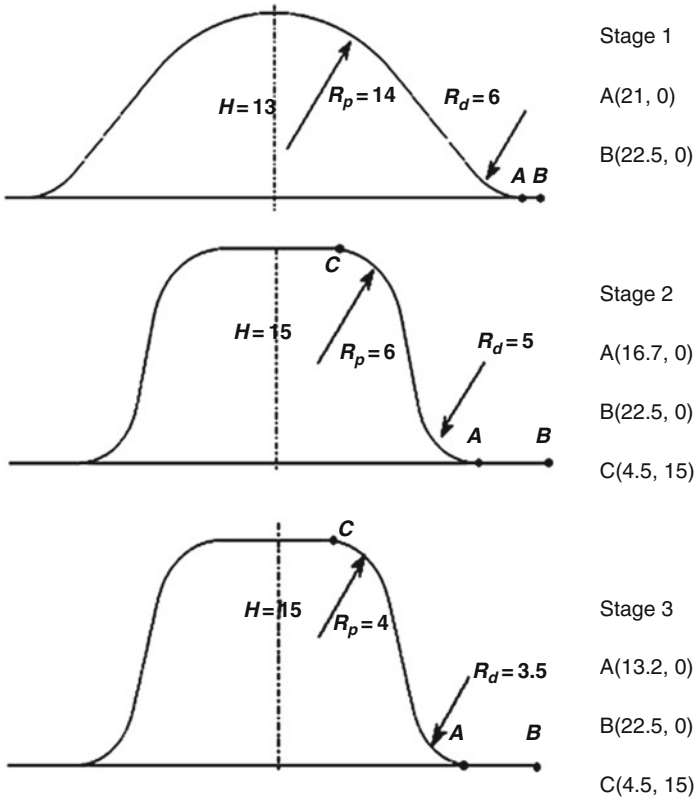

Fig. 18 Part geometry at the three stamping stages

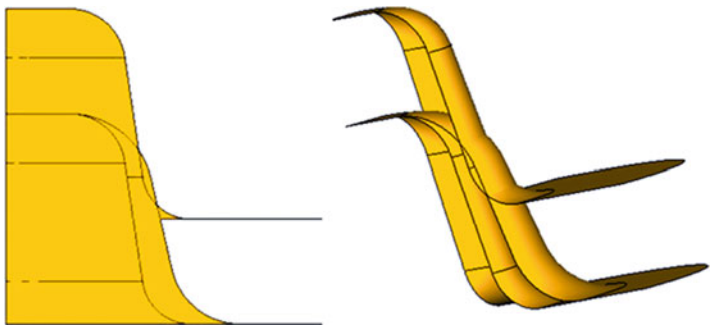

Fig. 19 Determination of the intermediate sheet shape in the third stage

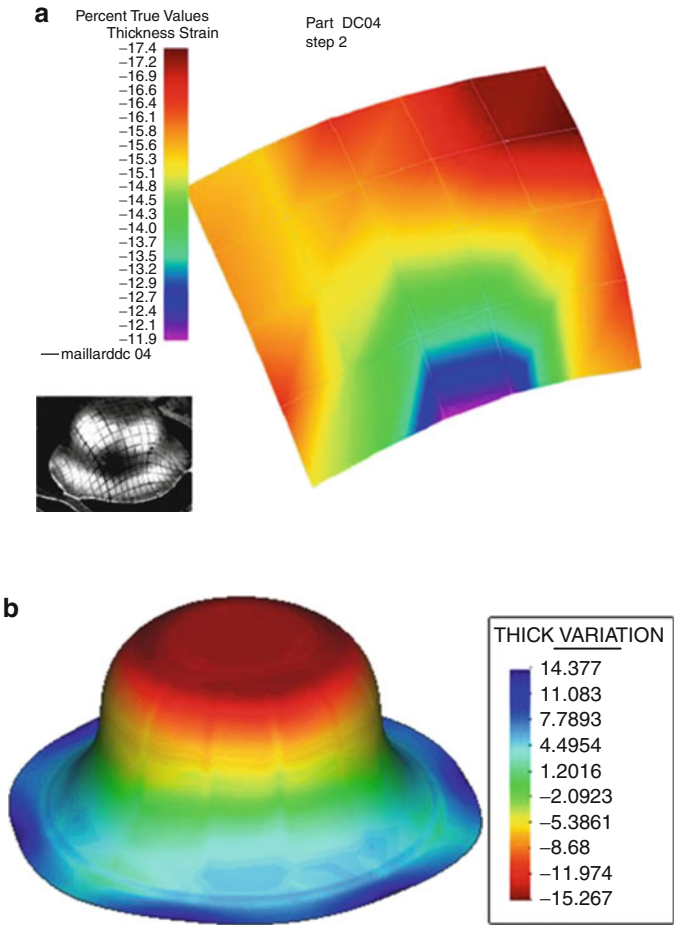

Fig. 20 Thickness variation (%) obtained by PIA and by test in stage 2. (**a**) Experimental test of CETIM. (**b**) Numerical simulation of PIA

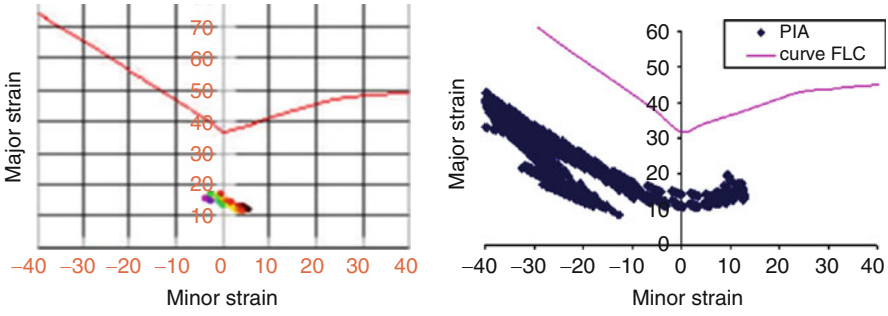

Fig. 21 FLC and FLD diagrams in stage 2

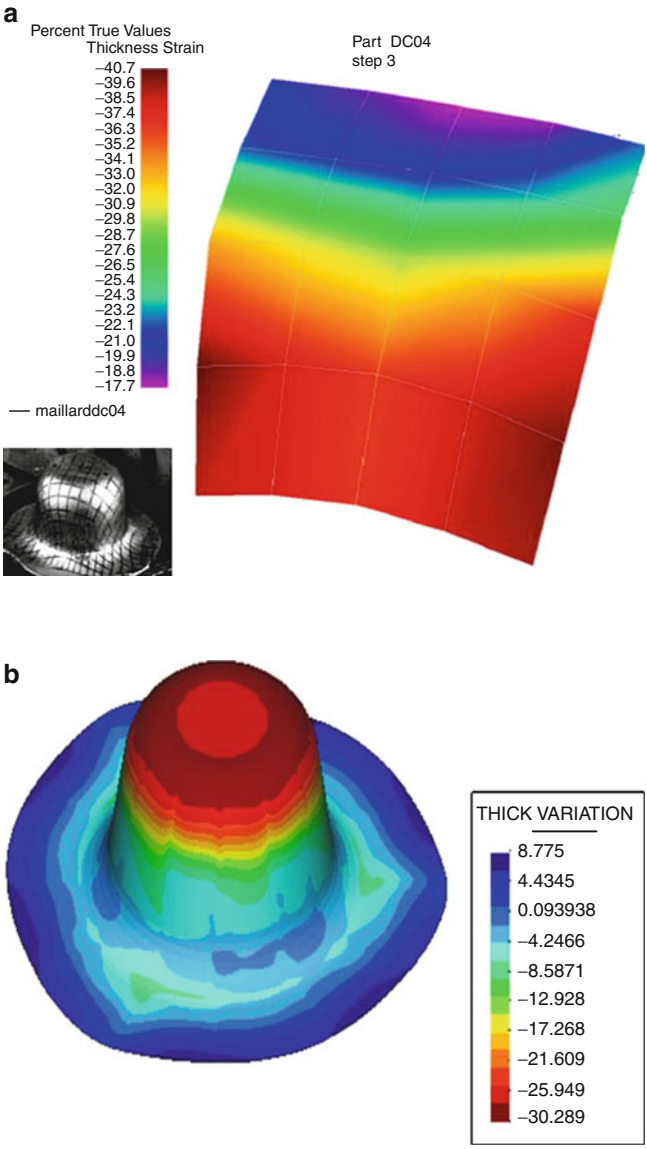

Fig. 22 Thickness variation (%) obtained by PIA and by test in stage 3. (**a**) Experimental test of CETIM. (**b**) Numerical simulation of PIA

contact-friction effects. Despite this difference, PIA is able to find correctly the maximal thinning zone.

In stage 3, the FLD numerical and experimental results are also fairly coherent (Fig. 23). In a "good part" just before the rupture, the points are very close to the FLC in both cases.

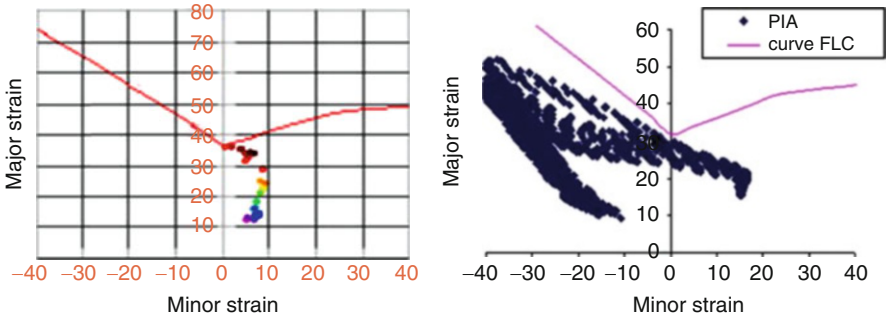

Fig. 23 FLC and FLD diagrams in stage 3

Simplified Plastic Ductile Damage Models and Direct Integration Algorithms

Strain-Based Damage Model

The damage models based on the continuum damage mechanics (CDM) were presented by (Chaboche 1988; Lemaître and Chaboche 1990). The damage effect is represented on the overall elastoplastic behavior of the material. This phenomenological model uses a scalar damage variable to describe the ductile defect evolution and thermomechanical behaviors. Advanced models on the CDM ductile damages and their strong couplings with elasto-viscoplastic behaviors are presented in ▶ Chap. 25, "Ductile Damage in Metal Forming: Advanced Macroscopic Modeling and Numerical Simulation". In the present chapter, a simplified damage model called "3D strain-based damage model" (Lemaître and Chaboche 1990) is used. This model partially ignores the loading history and is weakly coupled with the plastic behavior. It makes the formulation very simple and well adapted to the PIA, leading to an efficient numerical damage modeling.

The damage potential φ_D^* is chosen as the function of the strain energy density release rate $(-Y)$, so the damage rate $\dot{D}$ for a material with the isotropic hardening and damage can be written as follows:

$$\dot{D} = -\dot{\lambda}_D \frac{\partial \varphi_D^*}{\partial Y} = \left(\frac{-Y}{S_0}\right)^{s_0} \dot{\bar{\varepsilon}}^p \tag{31}$$

$$-Y = \frac{\sigma_{eq}^2}{2E(1-D)^2}\left[\frac{2}{3}(1+\nu) + 3(1-2\nu)\left(\frac{\sigma_{\mathrm{H}}}{\sigma_{eq}}\right)^2\right] \tag{32}$$

where $\dot{\lambda}_D$ is the damage multiplier rate, s_0 and S_0 are material coefficients in function of the temperature, σ_{eq} is the equivalent stress, σ_H is the hydrostatic stress, $\dot{\bar{\varepsilon}}^p$ is the equivalent plastic strain rate, E is Young's modulus, and ν is Poisson's coefficient.

Two assumptions are made to obtain a strain-based damage model: the assumption of hardening saturation after the damage threshold giving a perfect plasticity behavior and the assumption of proportional loading giving a constant triaxiality ratio σ_H/σ_{eq}.

Introducing the damage threshold ε_D, the equivalent plastic strain ε_R at the rupture, and the damage value at the rupture D_c (experimentally available, Zhu et al. 1992), a simplified strain-based damage model can be obtained in a rate form or in an integrated form:

$$\dot{D} = \frac{D_c}{\varepsilon_R - \varepsilon_D}\left[\frac{2}{3}(1+\nu) + 3(1-2\nu)\left(\frac{\sigma_H}{\sigma_{eq}}\right)^2\right]\dot{\bar{\varepsilon}}^p \quad ; \quad \text{if } (\bar{\varepsilon}^p > \varepsilon_D \text{ and } \sigma_H > 0) \tag{33}$$

$$D = \frac{D_c}{\varepsilon_R - \varepsilon_D}\left(\bar{\varepsilon}^p\left[\frac{2}{3}(1+\nu) + 3(1-2\nu)\left(\frac{\sigma_H}{\sigma_{eq}}\right)^2\right] - \varepsilon_D\right) \tag{34}$$

where $\dot{\bar{\varepsilon}}^p$ is the equivalent plastic strain rate, a compressive stress state ($\sigma_H < 0$) cannot induce the damage, giving $\dot{D} = 0$.

Constitutive Equations

In this chapter, the material is supposed to obey von Mises isotropic yield criterion (for cold forging) or Hill anisotropic yield criterion (for sheet forming). These criteria of plasticity with the damage consideration are given by

$$f = \frac{\sigma_{eq}}{1-D} - \bar{\sigma}(\bar{\varepsilon}^p) = 0 \tag{35}$$

with

$$\sigma_{eq} = \left(\boldsymbol{\sigma}^T \boldsymbol{P}\, \boldsymbol{\sigma}\right)^{1/2} \tag{36}$$

where $\bar{\sigma} = \bar{\sigma}(\bar{\varepsilon}^p)$ represents the uniaxial tensile curve, σ_{eq} is the equivalent stress, and $\boldsymbol{P}$ is isotropic or anisotropic matrix defined below.

The plastic normality rule is used as the flow rule to obtain the plastic strain rate:

$$\dot{\boldsymbol{\varepsilon}}^p = \dot{\lambda}\frac{\partial f}{\partial \boldsymbol{\sigma}} = \dot{\lambda}\frac{\partial f}{\partial \sigma_{eq}}\frac{\partial \sigma_{eq}}{\partial \boldsymbol{\sigma}} = \dot{\lambda}\frac{\boldsymbol{P}\,\boldsymbol{\sigma}}{(1-D)\sigma_{eq}} \tag{37}$$

Using the equivalent plastic work $\dot{\bar{\varepsilon}}^p \sigma_{eq} = (\dot{\boldsymbol{\varepsilon}}^p)^{\mathrm{T}}\boldsymbol{\sigma}$, the relation between the equivalent plastic strain rate and the plastic multiplier rate $\dot{\lambda}$ is obtained:

$$\dot{\bar{\varepsilon}}^p = \frac{1}{\sigma_{eq}}\frac{\dot{\lambda}\,\boldsymbol{\sigma}^T\boldsymbol{P}^T}{(1-D)\sigma_{eq}}\boldsymbol{\sigma} = \frac{\dot{\lambda}}{1-D} \tag{38}$$

The equivalent plastic strain is defined by

$$\dot{\bar{\varepsilon}}^{\,p} = (\dot{\boldsymbol{\varepsilon}}^{\boldsymbol{p}})^{\boldsymbol{T}} \boldsymbol{A}\, \dot{\boldsymbol{\varepsilon}}^{\boldsymbol{p}} \tag{39}$$

For the axisymmetrical cold forging, the isotropic material gives

$$\{\sigma\} = \begin{Bmatrix} \sigma_r \\ \sigma_\theta \\ \sigma_z \\ \sigma_{rz} \end{Bmatrix}; \quad \{\varepsilon\} = \begin{Bmatrix} \varepsilon_r \\ \varepsilon_\theta \\ \varepsilon_z \\ \varepsilon_{rz} \end{Bmatrix}; \quad \boldsymbol{P} = \begin{bmatrix} 1 & -0.5 & -0.5 & 0 \\ -0.5 & 1 & -0.5 & 0 \\ -0.5 & -0.5 & 1 & 0 \\ 0 & 0 & 0 & 3 \end{bmatrix};$$

$$\boldsymbol{A} = \frac{2}{3}\begin{bmatrix} 1 & 0 & 0 & 0 \\ 0 & 1 & 0 & 0 \\ 0 & 0 & 1 & 0 \\ 0 & 0 & 0 & 0.5 \end{bmatrix}$$

For the thin sheet forming, the assumptions of plane stress, transverse anisotropy, and isotropic hardening are adopted. Using the equivalent plastic work $\dot{\bar{\varepsilon}}^{\,p}\sigma_{eq} = (\dot{\boldsymbol{\varepsilon}}^{p})^{T}\boldsymbol{\sigma}$ and Eqs. 33, 35, the following relations in a local reference are obtained:

$$\{\sigma\} = \begin{Bmatrix} \sigma_x \\ \sigma_y \\ \sigma_{xy} \end{Bmatrix}; \quad \{\dot{\varepsilon}^{\mathrm{p}}\} = \begin{Bmatrix} \dot{\varepsilon}^{\mathrm{p}}_x \\ \dot{\varepsilon}^{\mathrm{p}}_y \\ \dot{\varepsilon}^{\mathrm{p}}_{xy} \end{Bmatrix}; \quad \boldsymbol{A} = \boldsymbol{P}^{-1} = \begin{bmatrix} 1 & \frac{-\bar{r}}{1+\bar{r}} & 0 \\ \frac{-\bar{r}}{1+\bar{r}} & 1 & 0 \\ 0 & 0 & \frac{2(1+2\bar{r})}{1+\bar{r}} \end{bmatrix}^{-1}$$

with the average transverse anisotropy coefficient $\bar{r} = \frac{1}{4}(r_0 + 2r_{45} + r_{90})$.

Integrated Constitutive Law

In the IA, the proportional loading assumption postulates that the stress tensor at a point is proportional to an initial tensor independent of the time:

$$\boldsymbol{\sigma}(\boldsymbol{x}, t) = \alpha(t)\boldsymbol{\sigma}(\boldsymbol{x}, t_0) \tag{40}$$

so the term $\boldsymbol{\sigma}/\sigma_{eq}$ is independent of the time and Eq. 37 can be analytically integrated:

$$\boldsymbol{\varepsilon}^{p} = \frac{\dot{\bar{\varepsilon}}^{p}}{\sigma_{eq}}\boldsymbol{P}\,\boldsymbol{\sigma} = \left(\frac{1}{E_S} - \frac{1}{E}\right)\boldsymbol{P}\,\boldsymbol{\sigma} \tag{41}$$

where the relation $\dot{\bar{\boldsymbol{\varepsilon}}}^{p} = \dot{\lambda}$ in Eq. 38 has been used (but without the damage consideration). Adding the elastic strain vector in Eq. 40, the total strain–stress relation is obtained:

$$\boldsymbol{\sigma} = \left[\boldsymbol{H}^{-1} + \left(\frac{1}{E_S} - \frac{1}{E}\right)\boldsymbol{P}\right]^{-1}\boldsymbol{\varepsilon} \tag{42}$$

where $\boldsymbol{H}$ is the elastic constitutive matrix. The damage effect is uncoupled with the plasticity and evaluated in the post-processing using Eq. 34.

Classical Return Mapping Algorithm for Plasticity–Damage

The elastic law coupled with damage can be written in a total or rate form:

$$\boldsymbol{\sigma} = (1 - D)\boldsymbol{H}\boldsymbol{\varepsilon}^{\mathrm{e}} \tag{43}$$

$$\dot{\boldsymbol{\sigma}} = (1 - D)\boldsymbol{H}(\dot{\boldsymbol{\varepsilon}} - \dot{\boldsymbol{\varepsilon}}^{\mathrm{p}}) - \frac{\dot{D}\boldsymbol{\sigma}}{1 - D} \tag{44}$$

While from Eqs. 33 and 38, the damage rate can be defined by

$$\dot{D} = \frac{\hat{Y}}{1 - D}\dot{\lambda} \tag{45}$$

with

$$\hat{Y} = \frac{D_c}{\varepsilon_R - \varepsilon_D}\left[\frac{2}{3}(1 + \nu) + 3(1 - 2\nu)\left(\frac{\sigma_H}{\sigma_{eq}}\right)^2\right] \tag{46}$$

Using Eqs. 37 and 44, 45, and 46, the stress rate can be expressed in function of the plastic multiplier rate $\dot{\lambda}$:

$$\dot{\boldsymbol{\sigma}} = (1 - D)\boldsymbol{H}\dot{\boldsymbol{\varepsilon}} - \dot{\lambda}\left(\frac{\boldsymbol{HP}}{\sigma_{eq}} + \frac{\hat{Y}}{(1 - D)^2}\boldsymbol{I}\right)\boldsymbol{\sigma} \tag{47}$$

Thus, the stress vector at the step n can be expressed in an incremental form:

$$\boldsymbol{\sigma}_n - \boldsymbol{\sigma}_{n-1} = (1 - D_n)\boldsymbol{H}\Delta\boldsymbol{\varepsilon} - \Delta\lambda\left(\frac{\boldsymbol{HP}}{\sigma_{eq,n}} + \frac{\hat{Y}}{(1 - D_n)^2}\boldsymbol{I}\right)\boldsymbol{\sigma}_n \tag{48}$$

where an implicit scheme is taken to ensure the numerical stability. Equation 44 can be rewritten as

$$\left(\boldsymbol{I} + \Delta\lambda\left(\frac{\boldsymbol{HP}}{\sigma_{eq,n}} + \frac{\hat{Y}}{(1 - D_n)^2}\boldsymbol{I}\right)\right)\boldsymbol{\sigma}_n = \boldsymbol{\sigma}_{n-1} + (1 - D_n)\boldsymbol{H}\Delta\boldsymbol{\varepsilon} \tag{49}$$

where the stress vector $\boldsymbol{\sigma}_n$ can be determined by using an elastic prediction then a plastic correction. The elastic prediction gives a trial stress state as follows:

$$\boldsymbol{\sigma}_n^{\mathrm{e}} = \boldsymbol{\sigma}_{n-1} + (1 - D_n)\boldsymbol{H}\Delta\boldsymbol{\varepsilon} \tag{50}$$

The above elastic stress vector is substituted into the plastic criterion (Eq. 35), noted as f^{e}. $f^{\mathrm{e}} < 0$ means the stress state inside the flow surface (elastic prediction is true), giving $\Delta\lambda = 0$; $f^{\mathrm{e}} > 0$ means the plasticity occurrence; a plastic correction

should be used to determine a new stress state on the flow surface ($f = 0$). In the Simo's return mapping method, one substitutes $\boldsymbol{\sigma}_n$ (in Eq. 49) into the plastic criterion (Eq. 35) and solves the nonlinear equation $f(\Delta\lambda) = 0$ by using the Newton–Raphson iterative method to obtain $\Delta\lambda$. It is noted that a weak coupling method between the damage and plasticity is often adopted by using the damage value D_n at the previous equilibrium iteration.

Direct Scalar Algorithm of Plasticity (DSAP) for Fast Plastic Integration

In this direct algorithm, using the equivalent stress operator, Eq. 45 with unknown stress vectors is transformed into a scalar equation in terms of the equivalent stresses which can be determined by using the tensile curve. Thus, a quadratic equation with an unique unknown $\Delta\lambda$ is obtained, leading to a direct solution.

Calculation of Approximate Ratio of the Elastic Strain Part in a Strain Increment

For a given strain increment, if the elastic and plastic parts can be separated (even approximately), the equivalent plastic strain $\overline{\varepsilon}_n^{\mathrm{p}} = \overline{\varepsilon}_{n-1}^{\mathrm{p}} + \Delta\overline{\varepsilon}^{\mathrm{p}}$ can be obtained, and then the equivalent stress can be calculated by using the tensile curve $\overline{\sigma}_n = \overline{\sigma}\left(\overline{\varepsilon}_n^{\mathrm{p}}\right)$.

In a loading increment, a material point may undergo an elastic unloading (*AD* in Fig. 24) and reloading (*DA*), and then an elastoplastic loading (*AC*) which is modeled numerically by an elastic prediction (*AB*) and plastic correction (*BC*). How can we determine the ratios of the elastic and plastic parts in a strain increment ($\gamma\Delta\boldsymbol{\varepsilon}$ and $(1-\gamma)\Delta\boldsymbol{\varepsilon}$)?

Supposing that the elastic part $\gamma\Delta\boldsymbol{\varepsilon}$ enables the stress state to reach the flow surface, the criterion of plasticity should be satisfied, leading to the following equations (Eq. 35):

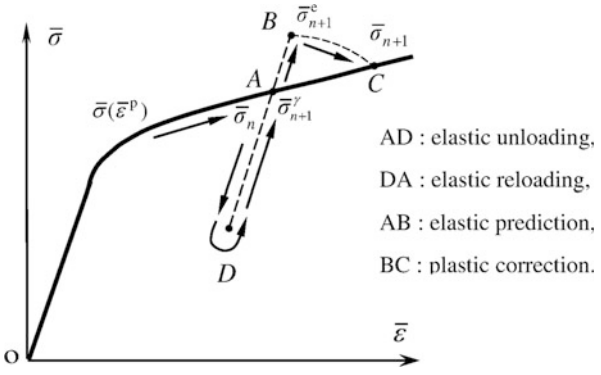

Fig. 24 Elastic unloading (*AD*), reloading (*DA*), and elastoplastic loading (*AC*)

$$\boldsymbol{\sigma}_n^{\gamma} = \boldsymbol{\sigma}_{n-1} + \gamma(1 - D_n)\boldsymbol{H}\Delta\boldsymbol{\varepsilon} \tag{51}$$

$$f\left(\boldsymbol{\sigma}_n^{\gamma}(\gamma)\right) = 0 \tag{52}$$

Equation 52 can be solved by the Newton–Raphson method. In order to avoid the iterative solution, the notion of the equivalent stress is adopted to transform Eq. 51 into a scalar equation by using the operation $\boldsymbol{\sigma}^T\boldsymbol{P}\boldsymbol{\sigma}$ at the two sides of Eq. 51:

$$\begin{aligned}\left(\sigma_{eq,n}^{\gamma}\right)^2 = \left(\sigma_{eq,n-1}\right)^2 &+ 2(1 - D_n)\gamma\boldsymbol{\sigma}_{n-1}^T\boldsymbol{P}\boldsymbol{H}\Delta\boldsymbol{\varepsilon} \\ &+ \gamma^2(1 - D_n)^2\Delta\boldsymbol{\varepsilon}^T\boldsymbol{H}\boldsymbol{P}\boldsymbol{H}\Delta\boldsymbol{\varepsilon}\end{aligned} \tag{53}$$

In the above equation, $\sigma_{eq,n}^{\gamma}$ and $\sigma_{eq,n-1}$ are determined by using the tensile curve, so γ can be obtained directly without iterations. The elastic ratio γ should be between 0 and 1. $\gamma > 1$ means that the total strain increment is insufficient to bring the stresses state back to the flow surface, so $\gamma = 1$ should be taken.

Once the elastic percentage γ is obtained, the equivalent plastic strain and equivalent stress at the step n can be calculated by

$$\overline{\varepsilon}_n^{\mathrm{p}} = \overline{\varepsilon}_{n-1}^{\mathrm{p}} + (1 - \gamma)\Delta\overline{\varepsilon}_n \tag{54}$$

$$\sigma_{eq,n} = (1 - D_n)\overline{\sigma}\left(\overline{\varepsilon}_n^{p}\right) \tag{55}$$

The stress $\sigma_{eq,n}$ will be used in Eq. 57 to calculate the plastic multiplier $\Delta\lambda$.

Direct Calculation of the Plastic Multiplier $\Delta\lambda$

In the plastic correction phase, Eqs. 49 and 50 can be rewritten as follows:

$$\boldsymbol{\sigma}_n^e = \left(\boldsymbol{I} + \Delta\lambda\left(\frac{\boldsymbol{HP}}{\sigma_{eq,n}} + \frac{\hat{Y}}{(1 - D_n)^2}\boldsymbol{I}\right)\right)\boldsymbol{\sigma}_n \tag{56}$$

By using the equivalent stress notion, the operation $\boldsymbol{\sigma}^T\boldsymbol{P}\boldsymbol{\sigma}$ is done on the two sides of the above equation, leading to an equation of second degree in $\Delta\lambda$:

$$\begin{aligned}\left(\sigma_{eq,n}^e\right)^2 = (\sigma_{eq,n})^2 &+ 2\Delta\lambda\,\boldsymbol{\sigma}_n^T\left(\frac{\boldsymbol{HP}}{\sigma_{eq,n}} + \frac{\hat{Y}}{(1 - D_n)^2}\boldsymbol{I}\right)\boldsymbol{P}\boldsymbol{\sigma}_n \\ &+ \Delta\lambda^2\boldsymbol{\sigma}_n^T\left(\frac{\boldsymbol{HP}}{\sigma_{eq,n}} + \frac{\hat{Y}}{(1 - D_n)^2}\boldsymbol{I}\right)^T\boldsymbol{P}\left(\frac{\boldsymbol{HP}}{\sigma_{eq,n}} + \frac{\hat{Y}}{(1 - D_n)^2}\boldsymbol{I}\right)\boldsymbol{\sigma}_n\end{aligned} \tag{57}$$

Normally, this nonlinear equation requires an iterative solution. However, if one uses the equivalent stress obtained by Eq. 55, the damage value D_n at the previous equilibrium iteration, and an approximate stress normal direction, then $\Delta\lambda$ can be directly obtained by solving Eq. 57 without iterations. Using the criterion of plasticity (Eq. 35) and the plastic normality flow rule, the normal of the flow surface can be determined by

$$\boldsymbol{n} = \frac{\partial f}{\partial \boldsymbol{\sigma}} = \frac{\boldsymbol{P}\boldsymbol{\sigma}}{(1-D)\sigma_{\mathrm{eq}}} \quad \rightarrow \quad \boldsymbol{n} = \frac{\boldsymbol{P}\boldsymbol{\sigma}_n}{(1-D_n)\sigma_{\mathrm{eq},n}} = \frac{\boldsymbol{P}\boldsymbol{\sigma}_n}{(1-D_n)^2\overline{\sigma}_n} \tag{58}$$

where the last known stress normal direction can be used. Finally, Eq. 57 can be simplified to a second-order equation of $\Delta\lambda$:

$$\begin{aligned}&\Delta\lambda^2\left[(1-D_n)^2\boldsymbol{n}^{\mathrm{T}}\boldsymbol{H}\boldsymbol{P}\boldsymbol{H}\boldsymbol{n} + \left(\frac{\hat{Y}}{(1-D_n)^2}\right)^2\left(\sigma_{\mathrm{eq},n}\right)^2 + 2\sigma_{\mathrm{eq},n}\hat{Y}\boldsymbol{n}^{\mathrm{T}}\boldsymbol{H}\boldsymbol{n}\right]\\ &+2\Delta\lambda\left[(1-D_n)^2\sigma_{\mathrm{eq},n}\boldsymbol{n}^{\mathrm{T}}\boldsymbol{H}\boldsymbol{n} + \frac{\hat{Y}}{(1-D_n)^2}\left(\sigma_{\mathrm{eq},n}\right)^2\right] + \left(\sigma_{\mathrm{eq},n}\right)^2 - \left(\sigma^{\mathrm{e}}_{\mathrm{eq},n}\right)^2 = 0\end{aligned} \tag{59}$$

It is noted that some quantities such as γ, $\boldsymbol{n}$, and D_n have been calculated approximately, an improvement can be done by replacing $(1-\gamma)\Delta\bar{\varepsilon}_n$ in Eq. 54 by $\Delta\lambda/(1-D)$ (Eq. 38) and repeat the operations of Eqs. 55 and 57 once again. But the numerical tests have shown a good agreement with the classical return mapping method even without this improvement.

This direct scalar algorithm to obtain $\Delta\lambda$ is very fast and robust; it enables to use large strain increments without divergence problems.

Numerical Results of Damage Prediction

Sheet Forming of a Square Box

An advanced fully coupled damage model is developed and implemented in ABAQUS/Explicit (Saanouni et al. 2000; Cherouat et al. 2004). This program is used to simulate the damage evolution in the sheet forming of a square box and to validate the PIA with the damage consideration.

The geometric data are as follows: initial blank 200 × 200 × 0.82 mm^3, punch section of 100 × 100 mm^2 with a round radius of 8 mm, and die cavity of 102.5 × 102.5 mm^2 with a round radius of 5 mm. The punch travel is 36 mm. The material properties are as follows: friction coefficient $\mu = 0.144$, Young's modulus $E = 210$ GPa, Poisson's coefficient $\nu = 0.3$, yield stress $\sigma_{\mathrm{y}} = 400$ MPa, and isotropic plasticity law $\overline{\sigma} = Q\left(1-e^{-b\bar{\varepsilon}}\right) = 1000\left(1-e^{-5\bar{\varepsilon}}\right)$ MPa. In the PIA, the used damage parameters ($D_c = 0.95$, $\varepsilon_R = 0.7$, $\varepsilon_D = 0$) give a similar damage behavior with that of Cherouat et al. (2004), but PIA damage model is not able to describe very large damage until the rupture. Figure 25 shows the damage distributions obtained by ABAQUS with coupled or uncoupled plasticity–damage models. It is found that the damage is always located in the same zone, but the damage value given by the coupled model is more concentrated and much bigger ($D_{\max} = 90.5$ %) in the coupled case than in the uncoupled case ($D_{\max} = 53.48$ %).

In Fig. 26, the damage distributions obtained by PIA are presented for the coupled and uncoupled cases. A similar phenomenon is observed, but the damage evolutions show some difference due to the different damage models: the rigidity in the ABAQUS simulation decreases more rapidly after the ultimate load.

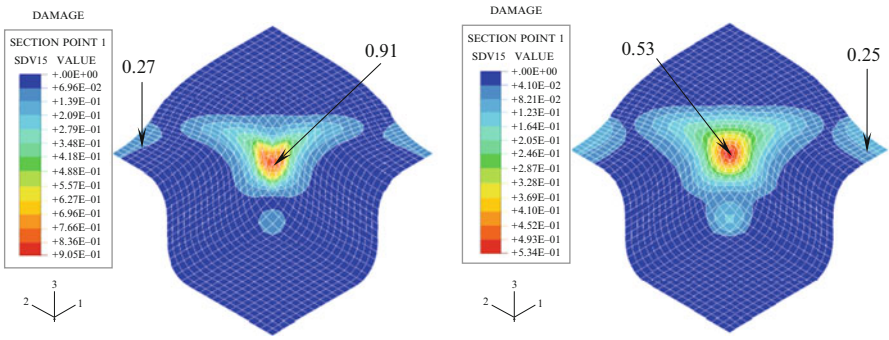

Fig. 25 Damage distributions by ABAQUS with advanced damage model. (**a**) Coupled damage–plasticity. (**b**) Non-coupled damage–plasticity

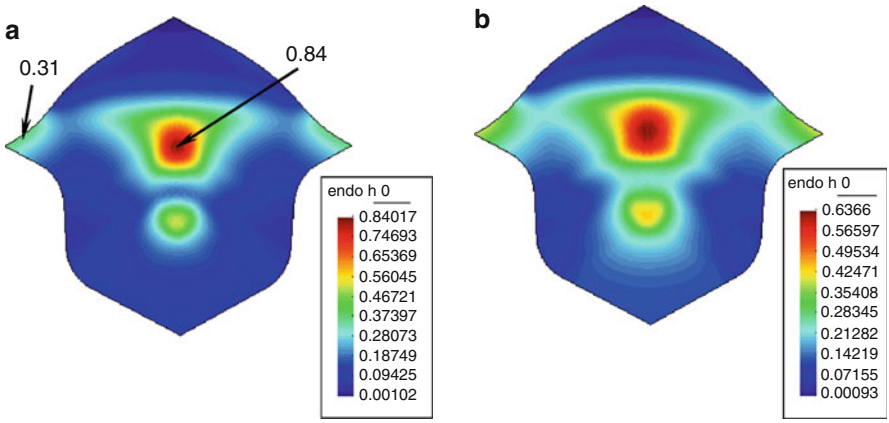

Fig. 26 Damage distributions by PIA with simplified strain-based damage model. (**a**) Coupled damage–plasticity. (**b**) Uncoupled damage–plasticity

SWIFT Stamping Simulation (Steel DC04)

This example is treated experimentally by CETIM and numerically by using the commercial code STAMPACK and the simplified PIA. Only eight steps are used for the PIA calculations. The geometry is presented in Fig. 27, and the material and process parameters are as follows: punch diameter $D = 33$ mm; die diameter $D_M = 35.2$ mm; friction coefficient $\mu = 0.144$; blank-holding force 500 daN; damage parameters for PIA $D_c = 0.4$, $\varepsilon_R = 0.7$, $\varepsilon_D = 0.2$; punch travel 14 mm; initial sheet diameter 74 mm; sheet thickness $t = 1$ mm; fillet radii $r_P = 5$ mm, $r_M = 4$ mm; Young's modulus $E = 82.377$ GPa; anisotropic coefficients $r_0 = 1.87$, $r_{45} = 1.12$, $r_{90} = 2.02$; and plastic behavior law $\overline{\sigma} = 559.66\left(\overline{\varepsilon}_p + 0.0057\right)^{0.226}$.

In Fig. 28, the FLC curves and FLD diagrams obtained by PIA and STAMPACK (without damage consideration) are presented. It is observed that these two codes give very similar FLD.

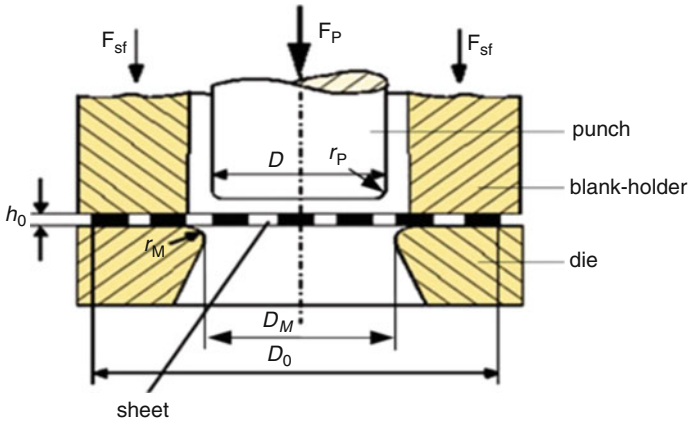

Fig. 27 Geometry of SWIFT stamping test

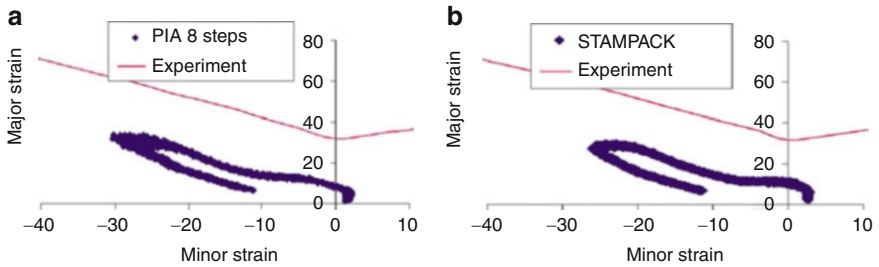

Fig. 28 FLD diagrams obtained by PIA and STAMPACK. (**a**) PIA eight steps. (**b**) STAMPACK

The damage distribution obtained by PIA is presented in Fig. 29. The strong damage zones are situated on the punch radius and on the die's entrance. The numerical results are in good agreement with the experimental results of CETIM. The rupture on the punch's radius and the necking on the die's entrance are clearly shown in the photo of CETIM.

Cold Forging of a Wheel

In this section, the cold forging modeling of a wheel is presented to show the efficiency and limitations of the PIA for the forging process. The results of the PIA including the strain-based damage model are compared to those obtained by the incremental approach ABAQUS/Explicit.

The geometry of the billet and punch is shown in Fig. 30. Due to the symmetry of the wheel, only a quarter of the part section is considered. The symmetric boundary conditions are imposed on the vertical axis and horizontal plane. To compare the two approaches, the final mesh obtained by ABAQUS® is taken for the PIA modeling, containing 1,402 nodes and 1,324 axisymmetric quadrangle elements. The tools are supposed rigid and modeled by analytic rigid wires.

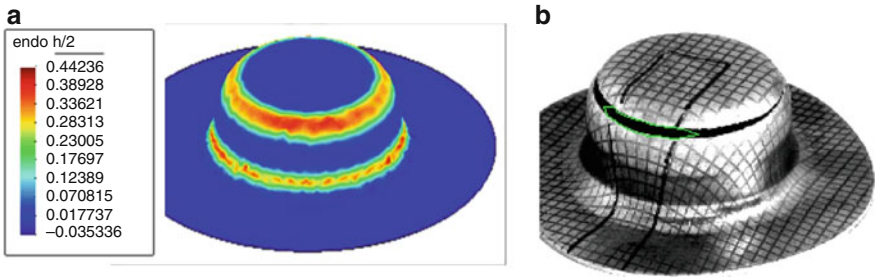

Fig. 29 Damage distribution obtained by PIA and rupture obtained by CETIM test. (**a**) Damage obtained by PIA. (**b**) Rupture in an experimental test

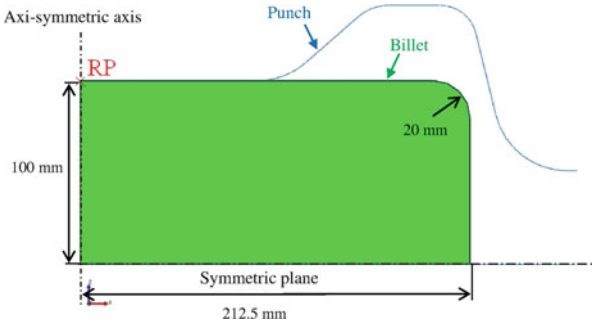

Fig. 30 Geometry of the billet and punch

The material properties of the billet in lead are Young's modulus $E = 17$ GPa, Poisson's ratio $\nu = 0.42$, friction coefficient $\mu = 0.05$, mass density $\rho = 11.35$ g/cm^3, and Hollomon strain–stress curve $\overline{\sigma} = 65.8(\overline{\varepsilon}^{p})^{0.27}$ MPa. The vertical punch travel is 38.8 mm. The damage parameters are $D_c = 0.5$, $\varepsilon_R = 0.315$ and $\varepsilon_D = 0.05$. Only 14 steps are needed for the PIA simulation, the results obtained by using more steps are almost unchanged.

Figure 31 shows the distributions of the equivalent plastic strain obtained by the PIA and ABAQUS®/Explicit. It is observed that the distributions are very similar and the maximal and minimal values are in good agreement between the two approaches.

The distributions of the equivalent stress obtained by the PIA and ABAQUS® are shown in Fig. 32. It is observed that the stress distributions are quantitatively very similar to each other. The maximum equivalent stresses are 57.59 MPa (PIA) and 57.49 MPa (ABAQUS®), respectively, giving an error of 0.2 %.

The damage distributions obtained by PIA and ABAQUS®/Explicit are presented in Fig. 33. It is found that the two approaches give very close damage values in the same zone: $D_{max} = 20.9$ % by the PIA and $D_{max} = 19.7$ % by ABAQUS®.

The PIA leads to a considerable gain of the CPU time compared to ABAQUS®. The ABAQUS®/Explicit uses 2,126 s, but the PIA uses only 460 s, saving 79 % of CPU time.

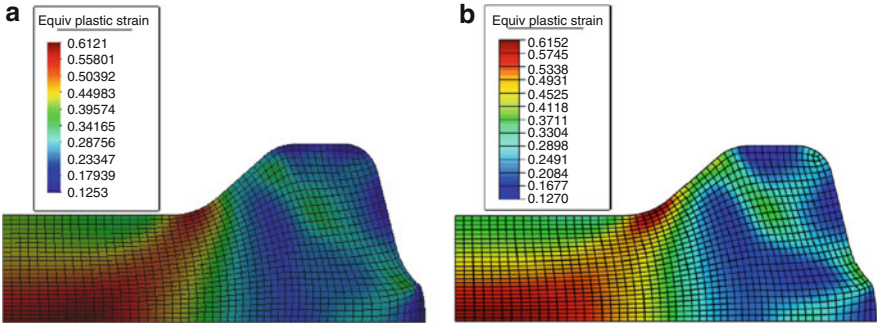

Fig. 31 Equivalent plastic strain distribution obtained by PIA and ABAQUS®. (**a**) Pseudo-inverse approach (14 steps). (**b**) ABAQUS® (339268 increments)

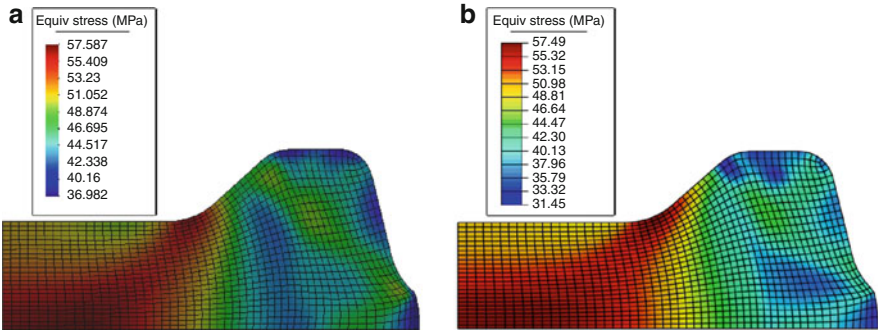

Fig. 32 Equivalent stress distribution obtained by PIA and ABAQUS®. (**a**) Pseudo-inverse approach (14 steps). (**b**) ABAQUS® (339268 increments)

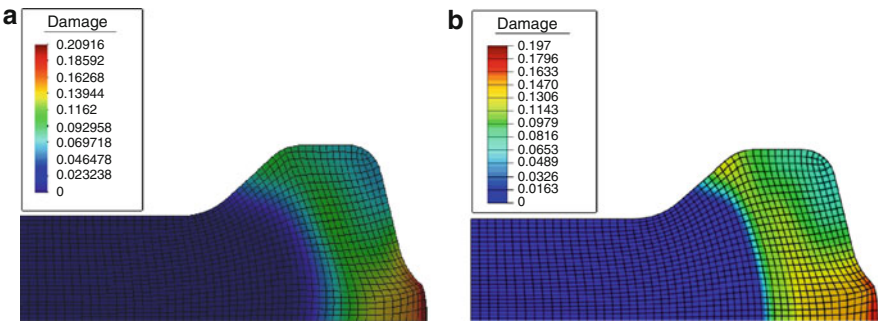

Fig. 33 Damage distributions obtained by PIA and ABAQUS®. (**a**) Pseudo-inverse approach (14 steps). (**b**) ABAQUS® (339268 increments)

Forming Process Optimization Using IA and PIA

General Aspects of the Forming Process Optimization

In a forming process, the original problem is usually a design or optimization problem. Firstly, its solution requires an accurate and efficient simulation of the process in multistages by an incremental or inverse method, taking into account the uncertainties, the affecting parameters, and the fine identification of material behaviors and interfaces. Secondly, the process and part geometry must be parameterized to reduce at maximum the computation time. Thirdly, global, robust, multi-objective, and parallel optimization algorithms should be used to find the optimal process and shape parameters.

The process optimization can largely improve the formability of the material and the robustness of the process. The combination of a numerical forming solver with an optimization algorithm allows an automatic design and control of process parameters, such as the material properties, the holding forces, the punch velocity and force, the geometry of the tools and initial billets, the addendum surfaces, the number and shapes of the forming tools, the friction aspects, the thermal effects, etc.

In the sheet forming field, many studies were presented on the optimization of forming process parameters such as the blank holding forces, the drawbead restraining forces, etc. (Jansson et al. 2005; Shim and Son 2000). Gelin et al. (2005) presented their works on the optimal design and control strategies for the sheet forming and tube hydroforming processes. Many works were done on the optimization of geometrical parameters such as the initial blank shape and the binder surface (Azaouzi et al. 2008, among others). Schenk and Hillmann (2004) proposed an approach for the design and optimization of addendum surfaces by changing the profile of the protection walls and the drawbead restraining forces. More recently, Dong et al. (2007) proposed an automatic procedure for the design and optimization of addendum surfaces by using the fast IA solver and the OpenCascade (2006) free library.

In the forging field, Kobayashi et al. (1989) firstly developed the backward tracing method for the preform design shape. Other groups worked on this method later and used it for the optimization procedure (Han et al. 1993). Zhao et al. (1997) presented an optimization method for the preform die shape design in metal forming processes. Fourment et al. (1996) and Vieilledent and Fourment (2001) made a great progress in this field. They developed shape sensitivity methods for the optimization of nonsteady-state forging processes; the preform shape was defined by B-spline curve taking the control points as design variables. Zhao et al. (2004) presented their studies on the multiple objective preform die shape optimal design by using the forward simulation and sensitivity analysis. Meng et al. (2010) worked on the multi-objective optimization of multistage forging by using advanced thermo-viscoplasticity-damage models and meta-models to optimize the tool shapes. Castro et al. (2010) worked on the optimization of shape and process parameters in metal forging using the genetic algorithms.

Halouani et al. (2012b) developed a fast forging solver called PIA for the multi-objective optimization of tool preform shapes.

For most of nongradient optimization algorithms (such as the response surface, the genetic method or simulated annealing), an important step is to carefully select a number of sampling points by a design of experiments (DOE). This selection has a great influence on the efficiency and accuracy of the optimization procedure. The DOE consists in selecting assessment of points in the design space. The difficulty is how to use the minimum points to obtain the best distribution of the sampling points. Several DOE can be found in the literature (Myers and Montgomery 2002). The well-known methods are the factorial design, central composite design, Latin hypercube, D-optimal, Box–Behnken, etc. A space-filling Latin hypercube design (LHD) is a good and popular DOE strategy for constructing meta-models from deterministic computer experiments (such as FE simulations) (McKay et al. 1979; Santner et al. 2003).

To limit the number of forming simulations, surrogate meta-models are often used to construct an approximate response surface based on the real simulation results for the optimal solution searching. In the literature, there are the moving least square method (Breitkopf et al. 2005; Naceur et al. 2010), the Kriging method (Emmerich et al. 2006), the diffuse approximation (Nayrolles et al. 1992), etc.

Since the metal forming processes involve very complicated phenomena, the multi-objective optimization with several constraints should be considered. The nongradient optimization algorithms are often adopted to avoid the gradient computation, to have a robust searching procedure, and to find global optimal solutions. Among the stochastic methods, the genetic algorithms and the simulated annealing algorithms are largely used (Fourment et al. 1996; Castro et al. 2010; Meng et al. 2010) to determine the Pareto front points and then to find the optimal solution according to other technological constraints. However, these algorithms are time-consuming; it is indispensible to reduce the number of design variables and to use a fast forming solver (Halouani et al. 2012b).

Optimization Procedure for Forming Processes

An optimization procedure comprises four steps: defining the objective functions, selecting the design variables, defining constraint functions, and finding the optimal design variables. The first three steps are denoted as the optimization "modeling." The fourth step is the optimization "solving" problem.

Design Variables

In metal forming processes, the design variables can be divided into geometrical, material and process-related variables. For the workpiece, the geometrical parameters are their shapes and dimensions; for the tools, the parameters are related to the die and punch geometries, including the holding part and drawbeads. The material parameters concern the Young's modulus, Poison coefficient, hardening behavior, anisotropy, damage, viscosity, etc. The process variables include the holding forces, punch travel and velocity, temperatures, friction, etc.

The shape optimization involves much more design variables than the process optimization. Since the computation time strongly depends on the number of design variables, so it is indispensible to parameterize the tools' geometries. This parameterization can be made by using segments and radii for the simple geometry such as the initial billet and final part (Meng et al. 2010). For more complicated geometry such as preforms, the B-spline curves and surfaces are adopted (Halouani et al. 2012).

Objective Functions

The optimization targets can be defined by multi-objective functions:

$$\begin{aligned} &\min[f_1(\boldsymbol{x}), f_2(\boldsymbol{x}), \ldots] \\ &\boldsymbol{x} = < x_1, x_2, \ldots, x_n >^{\mathrm{T}} \quad ; \quad x_{iL} \le x_i \le x_{iU}; \quad i = 1, 2, \ldots, n \end{aligned} \tag{60}$$

where $f_i(x)$ are the objective functions, x_i the design variables, and x_{iL} and x_{iU} the lower and upper bounds of the design variables.

Metal forming processes are very complicated, so the optimization procedure often involves several objective functions which depend on the forming process:

- Deep drawing: the objectives can be to minimize the thickness variation, reduce the number of forming stages, improve the surface aspect, minimize the springback, prevent the wrinkling or necking, minimize the blank weight, control the punch force, etc. The following objective function was proposed by Naceur et al. (2001) to minimize the thickness variation and avoid the necking and wrinkling:

$$f = \min \frac{1}{N_{elt}} \sum_{e=1}^{N_{elt}} \left(\frac{h^e - h^0}{h^0} \right)^p \tag{61}$$

where h^0 is the initial sheet thickness, h^e is the final thickness of an element, and p is a positive pair integer ($p = 2, 4, \ldots$).

- Forging: the objectives can be to optimize the grain sizes, reduce the punch force or forging energy, minimize the strain variance, avoid the folding, etc. The following objective function was used to minimize the strain variance (Meng et al. 2010; Halouani et al. 2012b):

$$f = min \frac{1}{V_t} \sum_{i=1}^{N_{elt}} V_i \left(\bar{\varepsilon}_i^{\mathrm{p}} - \bar{\varepsilon}_{\mathrm{avg}}^{\mathrm{p}} \right)^2 \quad \text{with} \quad \bar{\varepsilon}_{\mathrm{avg}}^{\mathrm{p}} = \frac{1}{V_t} \sum_{i=1}^{N_{elt}} V_i \bar{\varepsilon}_i^{\mathrm{p}} \tag{62}$$

where $\bar{\varepsilon}_i^{\mathrm{p}}$ is the equivalent plastic strain of the element i, $\bar{\varepsilon}_{\mathrm{avg}}^{\mathrm{p}}$ is the average equivalent plastic strain, V_i is the volume of the element i, and V_t is the total volume.

Constraint Functions

The constraints and objective functions are related to each other in the sense that they are often exchangeable. In an optimization modeling, one should decide which

quantity is selected as objective, which as constraint. For example, to avoid excessive thickness uniformity, the objective function (60) can be replaced by a constraint on the thinning and thickening. The implicit constraint functions are defined as follows:

$$g_i(\boldsymbol{x}) \leq 0 \qquad i = 1, 2, \ldots, n \tag{63}$$

In the case of the deep drawing, it is not allowed that the strain states exceed the forming limit curve (FLC). The constraint can be that all FLD points are situated below the FLC curve. In the case of forging, the constraint functions can be the conditions on the damage, wrinkling, filling, and volume (Meng et al. 2012; Halouani et al. 2012b): the maximal damage should be inferior to the damage threshold, the contour of the forged part should not have sudden changes (folding), the volume should remain constant, etc.

Optimization Algorithms

Five types of algorithms are often used for the forming process optimization: iterative algorithms, evolutionary and genetic algorithms, approximate optimization algorithms, adaptive optimization algorithms, hybrid and combined optimization algorithms.

(a) Iterative Algorithms

Optimization of metal-forming processes can be performed by using classical iterative algorithms (SIMPLEX, conjugate gradient, SQP, BFGS, etc.). These algorithms usually require the sensitivities of the objective function and constraint functions with respect to the design variables. In the case of metal forming, the FEM calculations are very time-consuming and may give inaccurate sensitivities. Generally, the iterative algorithms are inadaptable to the multi-objective optimization and may get trapped in local optima.

(b) Evolutionary and Genetic Algorithms

Genetic and evolutionary algorithms are promising because of their tendency to find the global optimum and the possibility for parallel computing. Furthermore, they do not require the sensitivity computation. However, the large number of function evaluations is a serious drawback. The non-dominated sorting genetic algorithm NSGA-II (Deb 2000) is appealing to many authors for the metal forming optimization.

(c) Approximate Algorithms

The response surface method (RSM) is a well-known representative of approximate optimization algorithms. RSM is based on fitting a low-order polynomial meta-model through real response points, which are obtained by running FEM calculations for some chosen design variable settings. Next to the RSM, other meta-modeling techniques are Kriging and neural networks. Allowing the parallel computing and avoiding the sensitivity calculation, the approximate optimization is a preferred technique for many authors. A disadvantage of these methods is that the result is an approximate optimum rather than the real global optimum.

(d) Adaptive Algorithms

Adaptive algorithms are incorporated within FEM codes and generally optimize the time-dependent load paths of the metal-forming process during each increment of the FEM calculation. For example, to optimize the time-dependent pressure load path in hydroforming, one should keep a sufficient pressure to avoid the wrinkling. When such risk is detected during a loading increment, the pressure is increased in the next increment to avoid wrinkles in the final product. The advantage of these algorithms is that the optimum is obtained in only one FEM simulation. However, the access inside the FEM software is necessary, and only time-dependent design variables can be considered. These disadvantages seriously limit the general applicability of these algorithms.

(e) Hybrid and Combined Algorithms

Many researchers tried to combine the advantages of different optimization algorithms. Within the metal forming community, most authors used approximate algorithms to establish a meta-model and adopted an iterative algorithm to find the optimum. Some others constructed relatively noisy meta-models (i.e., many local optima) by using the Kriging and neural networks techniques and then used a global genetic algorithm to solve the optimization problem. For adaptive optimization algorithms, certain choose iterative algorithms, others genetic ones. It is also possible to enhance an evolutionary algorithm with the information provided by a meta-model-based approximate algorithm to make it more efficient and to overcome the difficulty of the large number of function evaluations.

(f) Simulated Annealing Method

This stochastic optimization method was developed by Kirkpatrick et al. 1983. This method is derived from an analogy with the slow cooling phenomenon of a molten body, which leads to a low-energy solid state. It should slowly lower the temperature, marking long plateaus so that the body reaches the thermodynamic equilibrium at each temperature plateau. For materials, this low energy manifests itself by obtaining a regular structure, such as crystals in the steel. The analogy used by the simulated annealing is to search a physic state p minimizing the energy function $\Phi(p)$. Simulated annealing usually exploits the criteria defined by the algorithm of Metropolis et al. (1953) for the acceptance of a solution obtained by perturbation of the current solution. Theoretical studies show that the simulated annealing algorithm converges to a global optimum under certain conditions. The main drawback is related to the choice of numerous annealing parameters such as the initial temperature, the decay rate of the temperature, the stopping criteria, or the lengths of the temperature plateaus. These parameters are often chosen empirically.

Preform Design and Optimization

The two-stage cold forging of an axisymmetric wheel is simulated and optimized. The forging process is composed of a preforming stage using a preform tool (Fig. 34) and forging stage using the final tool given by the desired part (Fig. 35).

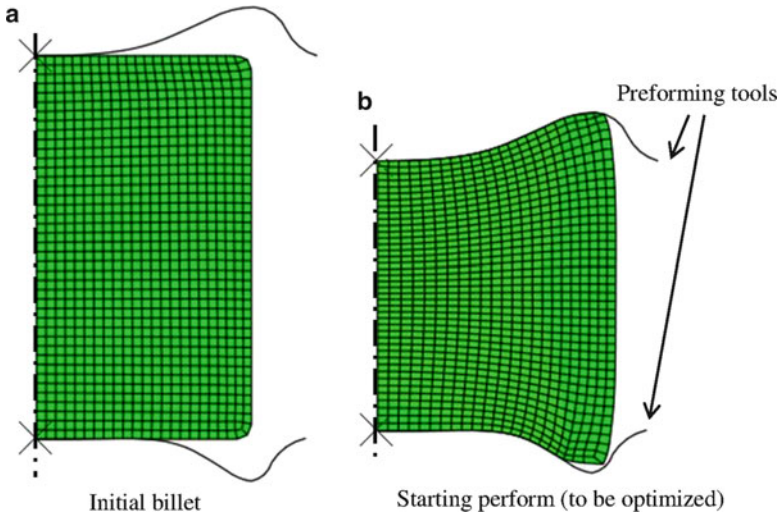

Fig. 34 Preforming stage using starting tool preform. (**a**) Initial billet. (**b**) Starting tool preform (to be optimized)

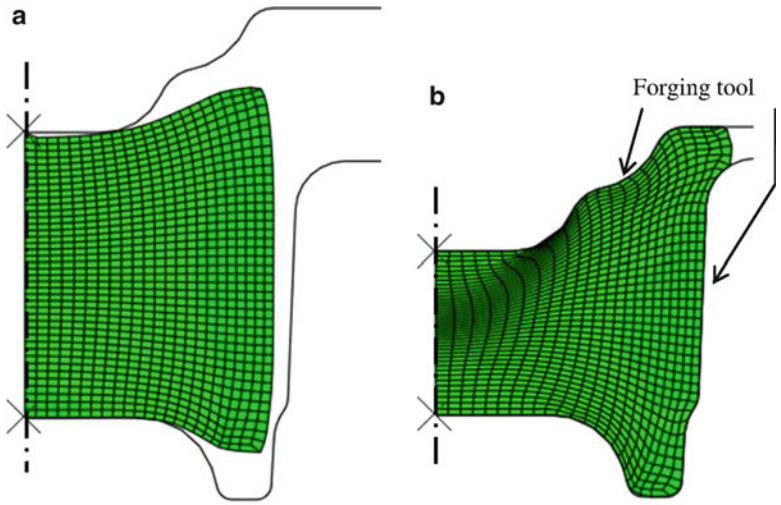

Fig. 35 Forging stage using preformed billet and final forging tools. (**a**) Billet obtained by performing stage. (**b**) Desired final forged part

The initial billet is a cylinder (height = 80 mm, radius = 45 mm). The geometry of the billet, the starting preform shape, and the final tools are shown in Figs. 34 and 35. The axisymmetric boundary conditions are imposed. The section is meshed with 830 nodes and 774 quadrilateral elements. The tools are supposed rigid and modeled by analytic rigid wires. The billet material is the lead: Young's modulus

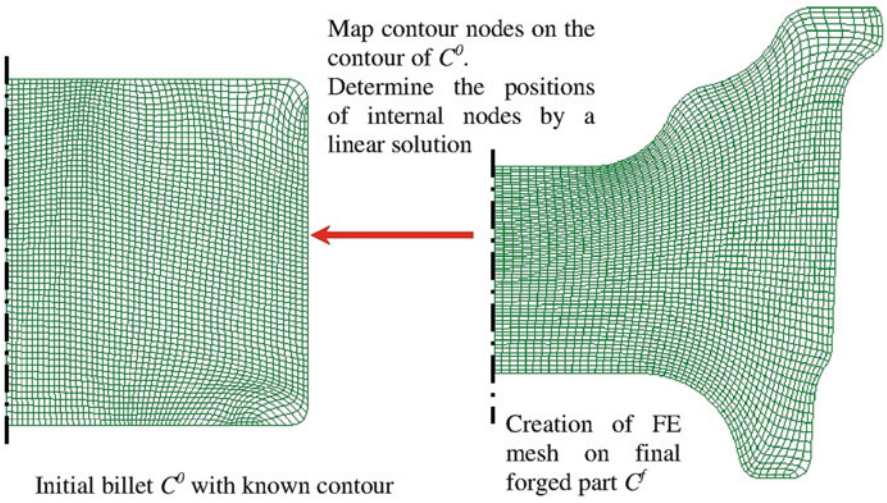

Fig. 36 FE mesh mapped from final part to initial billet

$E = 17$ GPa, Poisson's ratio $\nu = 0.42$, friction coefficient $\mu = 0.05$, and Hollomon tensile curve $\overline{\sigma} = 65.8(\overline{\varepsilon}^{\mathrm{p}})^{0.27}$ MPa.

In this work, the starting preform is created as follows:

1. Mesh mapping from the final forged part C^f to the initial billet C^0. A FE mesh is created on the known C^f, and the nodes at the contour of C^f are mapped on the contour of C^0; the positions of other nodes (interior nodes) in C^0 are determined by a linear solution with the imposed displacements on the contour (Fig. 36).
2. Creation of the geometrically proportional FE mesh between C^0 and C^f (Fig. 37): $\boldsymbol{X}_{\mathrm{p}}^1 = \boldsymbol{X}^f - (\boldsymbol{X}^f - \boldsymbol{X}^0)/2$.
3. Generation of a starting tool preform. The B-spline curve of this preform should fit well the proportional mesh contour except for the free surface part (Fig. 37). The right extremity (F) of the punch curve has the same height than that of the left extremity (E) and the same horizontal position than the maximal radial position (G) of the proportional preform. This choice gives a notable gap between the punch curve and preform shape on the zone B, but this gap has a little influence on the preform optimization. The B-spline curve of the lower die can be obtained by the same method.

A B-spline curve of the preform is defined by a polygonal contour having $n + 1$ ($n + 1 \geq 4$) control points $C_1 \ldots C_{n+1}$. These control points can be active or passive. Figure 38 shows the punch shape curve with seven control points; only their vertical displacements are taken as geometrical parameters to reduce the number of design variables. C_2 and C_6 are the passive points having the same vertical positions than C_1 and C_7 in order to keep the horizontal tangents at C_1 and C_7; other five are active points giving only five optimization design variables. The

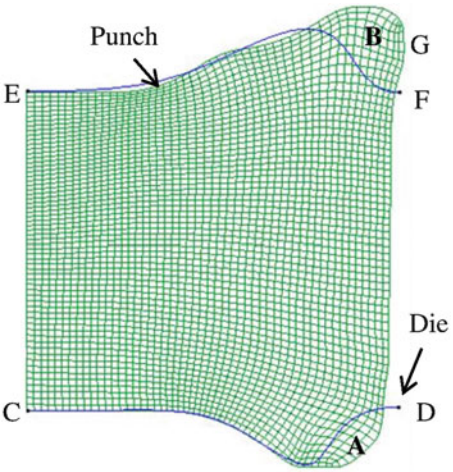

Fig. 37 Generation of proportional mesh and B-spline curves of the starting perform tools

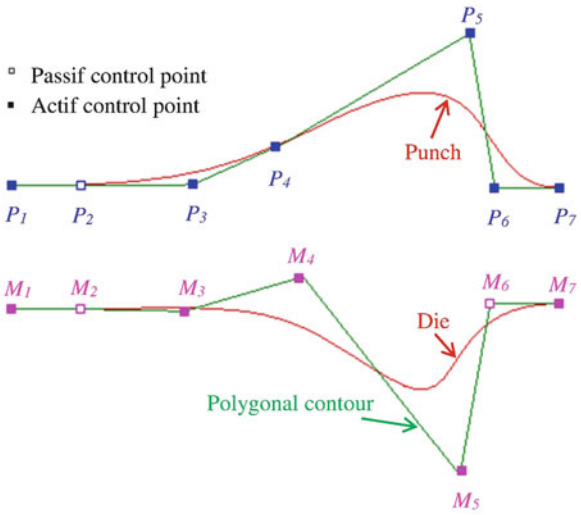

Fig. 38 Control points of the starting B-spline curves for preform tools

die shape curve is defined in same manner. Finally, there are only ten optimization design variables. These starting B-spline curves are then modified in the optimization loop to minimize the objective functions.

The validation of the PIA is done by using the software ABAQUS/Explicit. The punch travels are 23.7 mm in the preforming stage and 24.9 mm in the forming stage. The PIA is used firstly between the preform and initial billet, and then between the final part and preform. According to our numerical tests, the PIA results are no longer sensitive to the number of steps, from 11 steps for the preforming stage and from 12 for the forging stage.

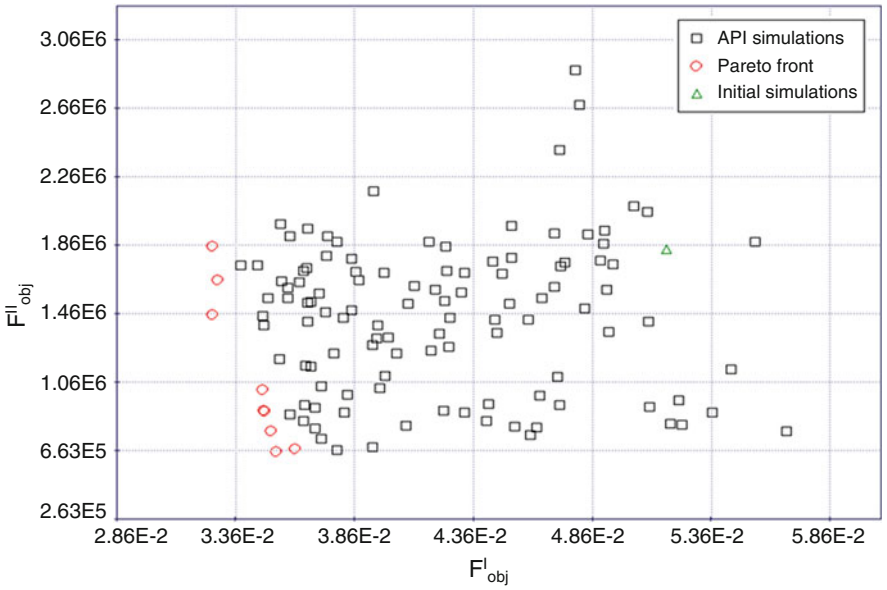

Fig. 39 Initial Pareto points obtained by using the real simulation results

In a multi-objective optimization, the concept of the best design is replaced by the concept of dominant design. This set of dominant designs is called Pareto frontier. The designer should find a good compromise for all objective functions according to other technical or economic constraints.

Two objective functions are adopted to minimize the plastic strain variation (Eq. 62) and the maximal punch force. A simulated annealing optimization algorithm called MOSA is used (ModeFRONTIER™ 4, User Manual). The initial Pareto points for this two-objective optimization problem are obtained by using 200 PIA simulations (or 200 iterations in the MOSA optimization loop). The distribution of these Pareto points (marked by red circles) is presented in the objective function plan ($F^{\mathrm{I}}_{\mathrm{obj}}$ and $F^{\mathrm{II}}_{\mathrm{obj}}$, Fig. 39).

The multi-objective optimization algorithms require a large amount of simulations, so it will be very expensive to minimize the objective functions entirely using real FE simulations. The Kriging method is adopted to build the surrogate meta-model for the two objective functions. Kriging method is a nonparametric interpolation model which interpolates the responses exactly at all sampling points. Figure 40 shows the surrogated metal-models of the two objective functions $F^{\mathrm{I}}_{\mathrm{obj}}$ and $F^{\mathrm{II}}_{\mathrm{obj}}$ using Gaussian Kriging method.

To get the optimal design values after building the meta-model, the genetic optimization algorithm called NSGA-II in the software modeFRONTIER™ is used. The distribution of the Pareto points obtained by using NSGA-II algorithm coupled with the Gaussian Kriging model is shown in Fig. 41. During the optimization, lots of new solutions are generated. This enables to have more optimal values on the

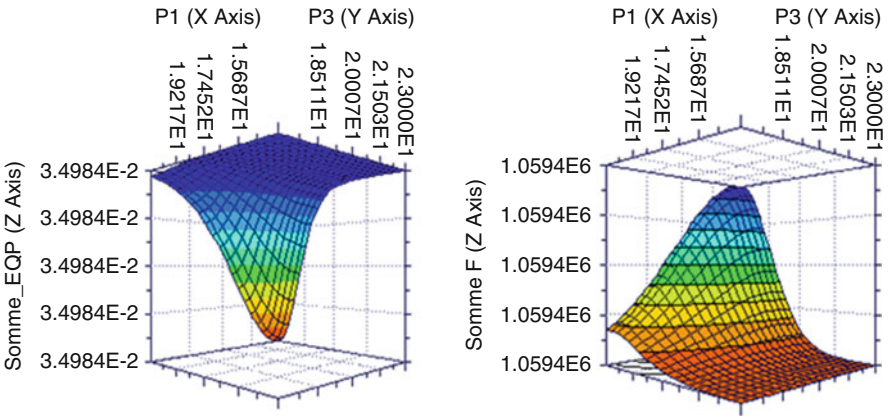

Fig. 40 Kriging surrogate meta-model of $F^{\mathrm{I}}_{\mathrm{obj}}$ and $F^{\mathrm{II}}_{\mathrm{obj}}$ in function of two design variables (vertical displacements of P1 and P3 in Fig. 38)

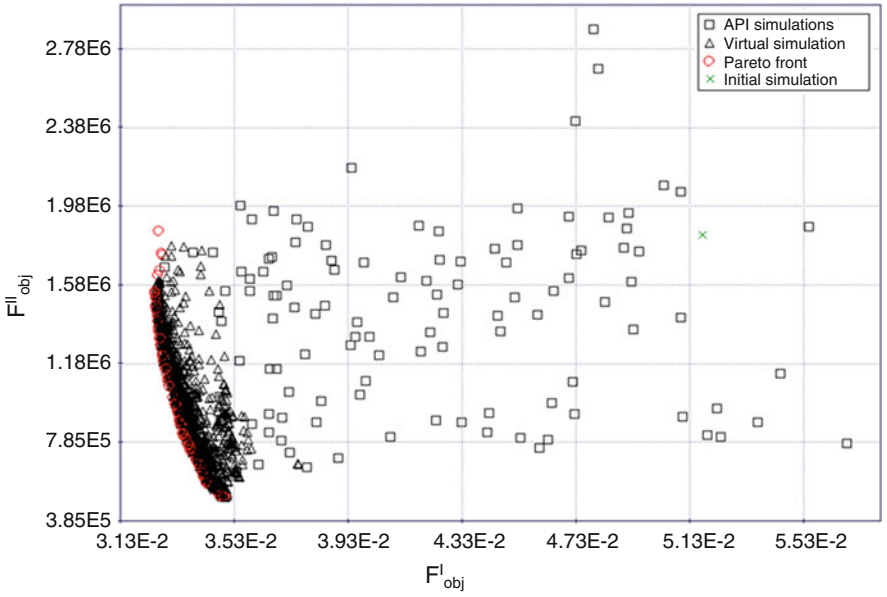

Fig. 41 Pareto front given by NSGA-II/Kriging

Pareto front, giving the final optimal solutions (marked by red circles in Fig. 41). It can be seen that the two objective functions largely decrease during the optimization ($F^{\mathrm{I}}_{\mathrm{obj}} = 0.052 \rightarrow 0.035$, $F^{\mathrm{II}}_{\mathrm{obj}} = 1842733.7 \rightarrow 504926.9$, Fig. 41), giving 33 % of reduction for the equivalent plastic strain and 72 % of reduction for the punch force.

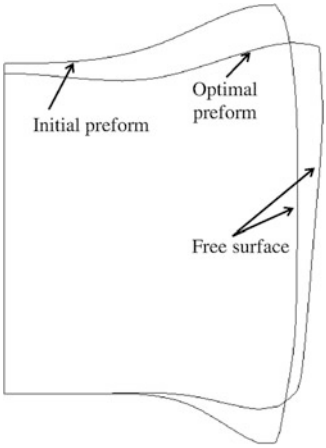

Fig. 42 Initial and optimal preform shapes

Figure 42 shows a comparison between the initial preform shape and the optimal one; a better result was achieved by using the proposed concept.

The CPU times for this two-stage forging simulation are also compared: the PIA uses only 285 s, but the ABAQUS/Explicit uses 1,453 s (5.1 times). Therefore, in the optimization procedure using 200 API simulations, the gain of the CPU time becomes enormous.

Conclusions

In this chapter, several simplified and practical approaches for damage prediction in metal-forming process modeling and optimization were presented.

- The IA exploits the knowledge of the final part shape and executes the calculation from the final part mesh to the initial blank or billet. The assumptions of proportional loading and simplified tool actions make the IA calculation very fast. This method gives fairly good strain estimation for the deep drawing, hydroforming, and cold forging processes, but poor stress evaluation. A simplified total strain-based damage model is implemented into the IA without considering the coupling effect between the plasticity and damage. The IA can be used as a numerical tool for the preliminary design and optimization in forming processes.
- The PIA is a good compromise between the IA and incremental approaches. The contact treatment is avoided by using some simplified tool actions as in the IA. In order to consider the strain path, some intermediate configurations are determined geometrically and corrected by using a surface minimization method or a free surface method, allowing very large strain increments. A 3D strain-based damage model in a rate form is adopted and coupled with the plasticity. An efficient direct scalar algorithm for damage–plasticity integration enables to take

into account the loading history so obtain good stress estimation. The PIA combines the advantages of the IA and incremental approaches: it gives better stress estimation then that of the IA and it is much faster than the incremental approach. The PIA is an efficient numerical tool for the damage prediction and forming processes optimization.

- The 3D strain damage model is based on the assumptions of the hardening saturation after the damage threshold and the proportional loading condition. It is implemented into the IA in a total form without considering its coupling with the plasticity. In the PIA, the model coupling the damage and plasticity is formulated and implemented in a rate form. The efficient direct scalar algorithm of plasticity (DSAP) for the integration of coupled damage–plasticity is developed to take into account the loading history. Using the notion of the equivalent stress, the constitutive equations in stress vectors are transformed into a scalar equation in which the equivalent stresses can be obtained by the tensile curve. Thus, the plastic multiplier can be obtained directly without iterations. This DSAP enables to largely reduce the CPU time and to avoid divergence problems even though for very large strain increments.
- Some optimization algorithms are combined with the IA using an integrated material law or with the PIA using the DSAP. These simplified methods make the optimization very efficient and robust, allowing to use the time-consuming optimization algorithms (such as genetic algorithm, simulated annealing method, etc.) in order to find globally optimal Pareto points for multi-objective functions.

Further research investigations will be devoted to continuously improve the original approaches IA and PIA. In the future, the authors will implement an adaptive meshing algorithm in the PIA in order to deal with complex parts undergoing very large plastic strains. In a forthcoming research, the authors will also include viscoplastic and thermomechanical material models in the PIA for the hot forging simulation. The fast PIA will be used to optimize tool preform shapes and other parameters of the forging process.

References

N. Aravas, The analysis of void growth that leads to central burst during extrusion. J. Mech. Phys. Solid **34**, 55–79 (1986)

M. Azaouzi, H. Naceur, A. Delameziere, J.L. Batoz, S. Belouettar, An heuristic optimization algorithm for the blank shape design of high precision metallic parts obtained by a particular stamping process. Finite Elem. Anal. Des. **44**, 842–850 (2008)

F. Barlat, J.C. Brem, J.W. Yoon, K. Chung, R.E. Dick, D.J. Lege, F. Pourboghrat, S.–.H. Choi, E. Chu, Plane stress yield function for aluminum alloy sheets–Part I: theory. Int. J. Plast. **19**, 1297–1319 (2003)

J.L. Batoz, G. Dhatt, *Modélisation des structures par éléments fini*, vol. 1, 3 (Edition HERMES, Paris, 1990)

P. Breitkopf, H. Naceur, A. Rassineux, P. Villon, Moving least squares response surface approximation: formulation and metal forming applications. Comput. Struct. **83**(17–18), 1411–1428 (2005)

M. Brunet, F. Sabourin, S. Mguil-Touchal, The prediction of necking and failure in 3d sheet forming analysis using damage variable. J. Phys. III **6**, 473–482 (1996)

F. Castro Catarina, C. António Carlos, C. Sousa Luisa, Pareto-based multi-objective hot forging optimization using a genetic algorithm, in *2nd International Conference on Engineering Optimization*, Lisbon, 2010

J.L. Chaboche, Continuum damage mechanics I-general concepts. II-damage growth, crack initiation, and crack growth. ASME Trans. J. Appl. Mech. **55**, 59–72 (1988)

M. Chebbah, H. Naceur, A. Gakwaya, A fast algorithm for strain prediction in tube hydroforming based on one-step inverse approach. J. Mater. Process. Technol. **211**(11), 1898–1906 (2011)

A. Cherouat, Y.Q. Guo, K. Saanouni, Y.M. Li, K. Debray, G. Loppin, Incremental versus inverse numerical approaches for ductile damage prediction in sheet metal forming. Int. J. Form. Process. **7**(1–2), 99–122 (2004)

J.P. Cordebois, P. Ladevèze, Necking criterion applied in sheet metal forming, in *Plastic Behavior of Anisotropic Solids*, ed. by J.P. Boehler (Editions CNRS, Paris, 1985)

K. Deb, An efficient constraint handling method for genetic algorithms. Comput. Method Appl. Mech. Eng. **186**(2–4), 311–338 (2000)

M. Dong, K. Debray, Y.Q. Guo, J.L. Shan, Design and optimization of addendum surfaces in sheet metal forming process. Int. J. Comput. Method. Eng. Sci. Mech. **8**(4), 211–222 (2007)

M. Emmerich, K. Giannakoglou, B. Naujoks, Single- and multiobjective evolutionary optimization assisted by Gaussian random field metamodels. IEEE Trans. Evolut. Comput. **10**(4), 421–439 (2006)

L. Fourment, T. Balan, J.L. Chenot, Optimal design for nonsteady-state metal forming processes – I shape optimization method. Int. J. Numer. Method Eng. **39**(1), 33–65 (1996)

J.C. Gelin, J. Oudin, Y. Ravalard, An imposed finite element method for the analysis of damage and ductile fracture in cold metal forming processes. Ann CIRP **34**(1), 209–213 (1985)

J.C. Gelin, C. Labergère, S. Thibaud, Recent advances in process optimization and control for the design of sheet and tube hydroforming processes, in Numisheet, Detroit, edited by L.M. Smith et al., Vol. A, pp. 825–830, 2005

Y.Q. Guo, J.L. Batoz, J.M. Detraux, P. Duroux, Finite element procedures for strain estimations of sheet metal forming parts. Int. J. Numer. Method Eng. **30**, 1385–1401 (1990)

Y.Q. Guo, W. Gati, H. Naceur, J.L. Batoz, An efficient DKT rotation free shell element for springback simulation in sheet metal forming. Comput. Struct. **80**(27–30), 2299–2312 (2002)

Y.Q. Guo, Y.M. Li, F. Bogard, K. Debray, An efficient pseudo-inverse approach for damage modeling in the sheet forming process. J. Mater. Process. Technol. **151**(1–3), 88–97 (2004)

A.L. Gurson, Porous rigid-plastic materials containing rigid inclusions – yield function, plastic potential and void nucleation, in *Proceedings of the Conference on Fracture*, vol. 2, pp. 357–364, 1977

A. Halouani, Y.M. Li, B. Abbès, Y.Q. Guo, An axisymmetric inverse approach for cold forging modelling. Eng. Lett. **18**(4), 376–383 (2010)

A. Halouani, Y.M. Li, B. Abbès, Y.Q. Guo, Simulation of axi-symmetrical cold forging process by efficient pseudo inverse approach and direct algorithm of plasticity. Finite Elem. Anal. Des. **61**, 85–96 (2012a)

A. Halouani, Y.M. Li, B. Abbès, Y.Q. Guo, F.J. Meng, C. Labergere, P. Lafon, Optimization of forging preforms by using pseudo inverse approach. Key Eng. Mater. **504–506**, 613–618 (2012b)

C.S. Han, R.V. Grandhi, R. Srinivasan, Optimum design of forging die shapes using nonlinear finite element analysis. AIAA J. **31**(4), 774–781 (1993)

P. Hartley, S.E. Clift, J. Salimi, C.E.N. Sturgess, I. Pillinger, The prediction of ductile fracture initiation in metalforming using a finite element method and various fracture criteria. Res. Mech. **28**, 269–293 (1989)

T. Jansson, A. Anderson, L. Nilsson, Optimization of draw-in for an automotive sheet metal part: an evaluation using surrogate models and response surfaces. J. Mater. Process. Technol. **159**(3), 426–434 (2005)

M. Jansson, L. Nilsson, K. Simonsson, Tube hydroforming of aluminium extrusions using a conical die and extensive feeding. J. Mater. Process. Technol. **198**(1–3), 14–21 (2008)
N. Kim, S. Kobayashi, Preform design in H-shape cross section axisymmetric forging by finite element method. Int. J. Mach. Tool Manuf. **30**, 243–268 (1990)
S. Kirkpatrick, C.D. Gelatt, M.P. Vecchi, Optimization by Simulated Annealing. Science, New Series. **220**(4598), 671–680 (1983)
S. Kobayashi, S.I. Oh, T. Altan, *Metal Forming and Finite Element Method* (Oxford University Press, Oxford, 1989)
C.H. Lee, H. Huh, Blank design and strain estimation for sheet metal forming processes by a finite element inverse approach with initial guess of linear deformation. J. Mater. Process. Technol. **82**, 145–155 (1998)
H. Lee, K.E. Peng, J. Wang, An anisotropic damage criterion for deformation instability and its application to forming limit analysis of metal plates. Eng. Fract. Mech. **21**(5), 1031–1054 (1985)
J. Lemaître, J.L. Chaboche, *Mechanics of Solid Materials* (Cambridge University Press, Cambridge, 1990)
Y.M. Li, B. Abbès, Y.Q. Guo, Two efficient algorithms of plastic integration for sheet forming modeling. ASME J. Manuf. Sci. Technol. **129**, 698–704 (2007)
J.F. Mariage, K. Saanouni, P. Lestriez, A. Cherouat, Numerical simulation of ductile damage in metal forming processes: a simple predictive model. Part I. Theoretical and numerical aspects. Int. J. Form. Process **5**(2–3–4), 363–376 (2002)
K. Mathur, P. Dawson, Damage evolution modeling in bulk forming processes, in *Computational Methods for Predicting Material Processing Defects* (Elsevier, Predeleanu, 1987)
M.D. McKay, W.J. Conover, R.J. Beckman, A comparison of three methods for selecting values of input variables in the analysis of output from a computer code. Technometrics **21**, 239–245 (1979)
F.J. Meng, C. Labergere, P. Lafon, Methodology of the shape optimization of forging dies. Int. J. Mater. Form **3**(Suppl 1), 927–930 (2010)
F. Meng, Multi-objective optimization of several stages forging by using advanced numerical simulation and Meta-model, PhD thesis, Université de Technologie de Troyes. (2012)
N. Metropolis, A.W. Rosenbluth, M.N. Rosenbluth, A.H. Teller, E. Teller, Equation of state calculations by fast computing machines. J. Chem. Phys. **21**, 1087–1092 (1953)
R. Myers, D. Montgomery, *Response Surface Methodology: Process and Product Optimization Using Designed Experiments*, 2nd edn. (Wiley, New York, 2002). ISBN 0-471-41255-4
H. Naceur, Optimisation de forme de structures minces en grandes transformations, Edition EUE, ISBN-13: 978-613-1-54700-3, p. 240, (2010)
H. Naceur, Y.Q. Guo, W. Gati, New enhancements in the inverse approach for the fast modeling of autobody stamping process. Int. J. Comput. Eng. Sci. **3**(4), 355–384 (2002)
H. Naceur, Y.Q. Guo, J.L. Batoz, C. Knopf-Lenoir, Optimization of drawbead restraining forces and drawbead design in sheet metal forming process. Int. J. Mech. Sci. **43**(10), 2407–2434 (2001)
H. Naceur, Y.Q. Guo, S. Ben-Elechi, Response surface methodology for design of sheet forming parameters to control springback effects. Comput. Struct. **84**, 1651–1663 (2006)
B. Nayrolles, G. Touzot, P. Villon, Generalizing the Finite Element Method: Diffuse approximation and diffuse elements. Comput. Mech. **10**, 307–318 (1992)
E. Onate, M. Kleiber, Plastic and viscoplastic flow of void containing metal – applications to axisymmetric sheet forming problem. Int. J. Numer. Meth. Eng. **25**, 237–251 (1988)
P. Picart, O. Ghouati, J.C. Gelin, Optimization of metal forming process parameters with damage minimization. J. Mater. Process. Technol. **80–81**, 597–601 (1998)
G. Rousselier, Ductile fracture models and their potential in local approach of fracture. Nucl. Eng. Des. **105**(1), 97–111 (1987)
K. Saanouni, *Damage Mechanics in Metal Forming. Advanced Modeling and Numerical Simulation* (ISTE/Wiley, London, 2012). ISBN 978-1-8482-1348-7

K. Saanouni, J.L. Chaboche, Computational damage mechanics, application to metal forming, in *Comprehensive Structural Integrity, Chapter 7*, ed. by R. de Borst, H.A. Mang. Numerical and Computational Methods, vol. 3 (Elsevier, Amsterdam, 2003)

K. Saanouni, K. Nesnas, Y. Hammi, Damage modeling in metal forming processes. Int. J. of Damage Mechanics. **9**(3), 196–240 (2000)

T. Santner, B. Williams, W. Notz, *The Design and Analysis of Computer Experiments* (Springer, New York, 2003)

O. Schenk, M. Hillmann, Optimal design of metal forming die surfaces with evolution strategies. Comp. Struct. **82**, 1695–1705 (2004)

H.B. Shim, K.C. Son, Optimal blank shape design by sensitivity method. J. Mater. Process. Technol. **104**, 191–199 (2000)

J.C. Simo, R.L. Taylor, A return mapping algorithm for plane stress elastoplasticity. Int. J. Numer. Method Eng. **22**, 649–670 (1986)

D. Vieilledent, L. Fourment, Shape optimization of axisymmetric preform tools in forging using a direct differentiation method. Int. J. Numer. Method Eng. **52**, 1301–1321 (2001)

G. Zhao, E. Wright, R.V. Grandhi, Preform die shape design in metal forming using an optimization method. Int. J. Numer. Method Eng. **40**(7), 1213–1230 (1997)

G. Zhao, X. Ma, X. Zhao, R.V. Grandhi, Studies on optimization of metal forming processes using sensitivity analysis methods. J. Mater. Process. Technol. **147**, 217–228 (2004)

Y.Y. Zhu, S. Cescotto, A.M. Habraken, A fully coupled elastoplastic damage modeling and fracture criteria in metal forming processes. J. Meter. Process. Technol. **32**, 197–204 (1992)